Fermi Search for Pulsar Wind Nebulae and constraints on the Galactic TeV source population

R. Rousseau, J. Lande, M. Lemoine–Goumard, S. Funk. . .

ABSTRACT

Since its launch, the *Fermi* satellite has firmly identified 7 pulsar wind nebulae (PWNe) plus a large number of candidates, all powered by young and energetic pulsars. Furthermore, PWNe are the most populous class in the TeV energy range followed by the unidentified sources (UNID). Using 45 months of Fermi–LAT data, we looked around the position of 56 TeV sources to bring new constraints on the models and new clues on the nature of sources without counterparts. For each of them we derived a γ–ray flux or an upper limit (when the TeV source is not detected at GeV energies by the *Fermi*–LAT) above 10 GeV.

The wealth of multi-wavelength data available and the new results provided by *Fermi*–LAT is an extraordinary opportunity to constrain the origin of the gamma-ray emission of the large sample of UNID and the radiative processes taking place in known PWNe.

Subject headings: Catalogs; Fermi Gamma-ray Space Telescope; Gamma rays: observations; pulsar wind nebula

1. Introduction

Since 2003, the continuous observation of the Galactic Plane by Čerenkov telescopes have yielded the detection of more than 80 Galactic sources. Among them, pulsar wind nebulae (PWNe) is the dominant class with more than 30 firm identifications. However, a similar number of Galactic sources cannot be associated to a counterpart in any other wavelength. They are ranked in the unidentified (UNID) class.

Multi-wavelength observations are essential to constrain the emission mechanisms occurring in these sources and identify their nature. The Large Area Telescope (LAT) aboard the *Fermi* Gamma-Ray Space Telescope (*Fermi*) is especially useful in this context. Covering the energy range from ~ 100 MeV to more than 300 GeV, the LAT provides a precise view of the γ-ray sky. With 2 years of observations, the *Fermi*–LAT Second Catalog (Nolan et al. 2012) already contains 1873 sources, 1397 being identified and 576 without counterparts.

[20] Two different scenarii are proposed to explain the observed γ-ray radiation : the accel-
erated particles are either electrons (leptonic scenario) or protons (hadronic scenario). In the
hadronic scenario, γ-ray photons are created by π^0 decay from the interaction of accelerated
hadrons with nuclei of the interstellar medium. In the leptonic scenario, γ-ray photons are
created by inverse Compton (IC) scattering of the accelerated leptons on the ambient photon
fields (CMB, Stellar Radiation, IR, ...).

[26] Leptonic sources such as relic PWNe (de Jager & Djannati-Ataï 2009; de Jager et al.
2009) and hadronic sources such as old supernova remnants interacting with molecular clouds
(Uchiyama 2011) have been proposed to explain the population of unidentified sources.

[29] The distinction between these two scenarii is done by studying the link between the
TeV and the GeV energy range. Slane et al. (2010); Grondin et al. (2011); Rousseau et al.
(2012) have demonstrated the potential that can be provided by the use of LAT observations
to study PWNe candidates. Up to now, except Vela–X (Abdo et al. 2010c), the 7 PWNe
firmly identified by Fermi are all associated to a TeV counterpart and show a hard spectrum
consistent with an IC peak above 100 GeV (Abdo et al. (2010b),Grondin et al. (2011)).

[35] The motivation of this work is to bring new constraints on already known PWNe and
to look for new candidates among the unidentified TeV sources. A search for gamma-ray
emission in the off-pulse window of the γ-ray detected pulsars, updating the method proposed
in Ackermann et al. (2011), will be presented in **cite 2PC**. The strategy presented in our
work (this paper) is closer to Tam et al. (2010) in the sense that we analyzed the *Fermi*-LAT
data around already known potential PWNe.

[41] The sources included in our search were detected by H.E.S.S., VERITAS, MAGIC and
MILAGRO. H.E.S.S. (Aharonian et al. 2006c) is composed of four telescopes observing the
very high energy (VHE) sky from 0.1 to 100 TeV with a mean point spread function (PSF) of
$\sim 0.1°$ for a point–source sensitivity around 1% of the Crab flux above 200 GeV for 25 hours
of observations. The four telescopes of VERITAS (Weekes et al. 2002) detect the ~ 0.1 to
30 TeV γ-rays with a sensitivity of 1% of the Crab in less than 30 hours and an angular
resolution lower than $0.1°$ at 1 TeV. MAGIC (Aleksić et al. 2012) consists of two telescopes
observing from ~ 50 GeV to several tens of TeV with a sensitivity of $\sim 0.8\%$ of the Crab
nebula flux above 300 GeV with a $\sim 0.1°$ PSF. MILAGRO (Abdo et al. 2007a) is a water
Čerenkov detector with a large field of view (FoV) of ~ 2sr and a $\sim 0.45°$ angular resolution
observing γ-rays from ~ 1 to 100 TeV.

[52] Starting from the TeV catalog website [1], which summarizes all sources detected at TeV

---

[1]http://tevcat.uchicago.edu/

energies, we established a list of sources possibly associated to PWNe (Section 3), that we studied using the method and the tools described in Section 4. The spatial and spectral results (Section 5) will be presented in the context of a population study (Section 6) before discussing the case one by one (Section 7). **a remoduler une fois le reste fait.**

2. LAT Description and Observations

The LAT is a γ-ray telescope that detects photons by conversion into electron-positron pairs and operates in the energy range between 20 MeV and more than 300 GeV. Details of the instrument and data processing are given in Atwood et al. (2009). The on-orbit calibration is described in Abdo et al. (2009c).

The following analysis was performed using 45 months of data collected from August 4, 2008 to Mai 18, 2012 (MET : 239557440–356439741) within a $7°\times7°$ square (see section 4) around the position of the TeV source aligned with Galactic coordinates. We excluded γ-rays coming from a zenith angle larger than 100° because of possible contamination from secondary γ-rays from the Earth's atmosphere (Abdo et al. 2009b). We used the Pass 7 clean event class that has a substantial reduction in instrumental background above 10 GeV with only a small loss in effective area (compared to the standard event class).

This energy of 10 GeV is a good compromise between photon statistics, angular resolution necessary to study the shape of the TeV sources and proximity to the energy range covered by the $\check{C}$erenkov telescopes. This also greatly reduces the contribution of the Galactic diffuse background.

The counts map in Figure 1 summarizes the regions of the Galactic Plane analyzed here. The bright pulsars Vela and Geminga clearly stand out, as well as the SNR IC443. In addition to these famous objects, a large number of sources clearly appears along the Galactic Plane, several of them being coincident with TeV detected sources, such as HESS J1614−518 and HESS J1616−508. They will be discussed in Section 5. The large number of sources visible in this counts map highlight perfectly the capabilities now offered at high energy by the LAT.

3. List of candidates

As a starting point, we used the catalog of TeV sources provided by the university of Chicago[1] to build our list of candidates. This catalog summarizes the information of all sources detected by the TeV experiments. Looking for PWNe candidates which are galactic

⁸⁴ sources, we selected the sources located within $\pm 5°$ in latitude.

⁸⁵ The Galactic center being a complex region to study with *Fermi*–LAT data, due to
⁸⁶ contamination by the large density of sources and by the diffuse emission, we removed all
⁸⁷ sources within $5°$ of the Galactic center. Thus, we did not include to our list the three sources
⁸⁸ HESS J1745-303, HESS J1741-302 and G 0.9+0.1 **citer Lola + autre papier venant sur**
⁸⁹ **les SNRs**.

⁹⁰ TeV sources associated to SNRs will not be discussed in this analysis. These sources
⁹¹ will be included in a forthcoming paper which aims at bringing constraints on all known
⁹² SNRs using the *Fermi*–LAT data **(cite the SNR cat)**.

⁹³ Finally we removed from this analysis the Crab Nebula and Vela-X. Both were already
⁹⁴ studied in details (Abdo et al. (2010b), Buehler et al. (2012)), and the second is the object
⁹⁵ of a new analysis **Grondin et al., Forthcoming**.

⁹⁶ The final list of 56 sources studied in this analysis is summarized in Table **??** together
⁹⁷ with their morphology as seen in TeV.

4. Conventions and methods

4.1. Modeling of the regions of interest

¹⁰⁰ Two different tools were used to perform the spatial and spectral analysis: `gtlike`
¹⁰¹ (Mattox et al. 1996) and `pointlike` (Kerr 2011; Lande et al. 2012). These tools fit a source
¹⁰² model to the data along with models for the instrumental, extragalactic and Galactic com-
¹⁰³ ponents of the background. We used the version 09–28–00 of the *Fermi* Science Tools.

¹⁰⁴ `pointlike` and `gtlike` using two different shapes for the region of interest, we used all
¹⁰⁵ events contained in a disk of $5°$ centered on the location of the TeV source when fitting the
¹⁰⁶ region with `pointlike` and we used a $7° \times 7°$ square included in the previous disk when fitting
¹⁰⁷ the region using `gtlike`. We tried to keep the two methods as close as possible by using
¹⁰⁸ the same conventions (same spatial binning : $\sim 0.06°$/bin, same energy binning : 8 energy
¹⁰⁹ bins per decade between 10 GeV and 316 GeV, same optimizer : MINUIT (James & Roos
¹¹⁰ 1975)).

¹¹¹ In the following analysis, the Galactic diffuse emission was modeled by the standard
¹¹² LAT diffuse emission ring−hybrid model *ring_2yearp7v6_v0.fits* for all sources. The residual
¹¹³ cosmic-ray background and extragalactic radiation are described by a single isotropic compo-
¹¹⁴ nent with a spectral shape described by the file *isotrop_2year_P76_clean_v0.txt*. The models

have been released and described by the *Fermi*-LAT Collaboration through the FSSC[2]. In the following, we fixed the isotropic diffuse normalization to limit the number of free parameters and reduce the uncertainties on the fitted parameters.

Sources within $10°$ around each source of interest and listed in the hard source list **(cite the hard source list paper)** were included in our spatial-spectral model. We replaced potential TeV counterparts by a source with the TeV morphology summarized in Table 1. The spectral parameters of sources closer than $2°$ to the source of interest were left free, while the parameters of all other sources were fixed at the hard source list (1FHL) catalog values.

Table 2 summarizes the sources of our list located close to a pulsar detected by the *Fermi*-LAT **cite 2PC**. The proximity of the pulsar can lead either to the non detection of a faint source hidden by the pulsed emission or to a contamination at low energy if the pulsar is not included. We decided to include in our analysis all the pulsars if they were outside of the TeV template or if they were more than $0.27°$ away from the source of interest. Section **??** will show the results for the sources close to the pulsars in the case were we added the pulsar in the model and fitted the TeV source.

Due to the longer integration time of our analysis with respect to the 1FHL catalog (45 vs 36 months in the 1FHL), the appearance of additional sources is expected. To prevent contamination from these sources, we looked over all our regions and added to the model all excesses with a significance above $4.0\ \sigma$ which corresponds to a TS > 25 with 4 degrees of freedom (2 spatial and 2 spectral, see Section 4.4). The location and spectral parameters of theses sources are described in Table 3. We fitted their spectra assuming a pure power–law above 10 GeV.

4.2. Analysis of the shape

Estimation of the position and extension of each PWNe candidates was performed using `pointlike`. `pointlike` is an alternate binned likelihood technique, optimized for characterizing the extension of a source (unlike `gtlike`), that was extensively tested against `gtlike` (Kerr 2011; Lande et al. 2012). To fit an extended source, `pointlike` convolves the extended source shape with the PSF (as a function of energy) and uses the MINUIT library (James & Roos 1975) to maximize the likelihood by simultaneously varying the position, extension, and spectrum of the source. Lande et al. (2012) present more details on the method

---

[2]http://fermi.gsfc.nasa.gov/ssc/data/access/lat/BackgroundModels.html

146 used and its validation.

147 As previously done in Lande et al. (2012), we only used radially-symmetric uniform disk
148 shape (defined in Equation 1) to fit the extension of the GeV emission. In the following, we
149 quote the radius to the edge (σ) as the size of the source.

$$I_{\text{disk}}(x,y) = \begin{cases} \frac{1}{\pi\sigma^2} & x^2 + y^2 \leq \sigma^2 \\ 0 & x^2 + y^2 > \sigma^2. \end{cases} \tag{1}$$

4.3. Spectral analysis

151 We performed the spectral analysis of each TeV candidate using `pointlike` and `gtlike`,
152 the standard likelihood analysis package for LAT data implemented in the Science Tools
153 and distributed by the FSSC. It is a binned maximum-likelihood method (Mattox et al.
154 1996) that was extensively validated for spectral analysis and makes fewer approximations
155 in calculating the likelihood than `pointlike`. Both methods provided results in agreement
156 with each other, but all spectral parameters quoted in the following were obtained using
157 `gtlike`. The spectrum of each source was determined using the best morphological model
158 provided by `pointlike`. Due to the narrow energy range which prevents the detection of
159 curved spectra, we fitted all sources assuming a pure power-law of differential flux K and
160 index Γ presented in Equation 2.

$$\frac{dN}{dE} = K \times \left(\frac{E}{E_0} \right)^{\Gamma} \tag{2}$$

161 To minimize the covariance between K and Γ, we ran the whole analysis twice. In the
162 first iteration, we fitted the source assuming a power-law model depending on the integral
163 flux N and Γ shown in Equation 3.

$$\frac{dN}{dE} = \frac{N \times (\Gamma + 1) \times E^{\Gamma}}{E_{max}^{\Gamma+1} - E_{min}^{\Gamma+1}} \tag{3}$$

164 Using the covariance matrix between the parameters of the fit, we derived the pivot
165 energy E_p computed as the energy at which the relative uncertainty on the differential flux
166 K was minimal (Nolan et al. 2012). Then, we refitted the spectrum of the source assuming
167 a power-law spectral model (Equation 2) with the scale parameter E_0 fixed at E_p.

168 Once the morphological and spectral fit was determined, we derived the photon flux

F(10–316 GeV) in photons cm^{-2} s^{-1} and the energy flux G(10–316 GeV) in erg cm^{-2} s^{-1} defined as:

$$F(10 - 316\,\mathrm{GeV}) = \int_{10\mathrm{GeV}}^{316\mathrm{GeV}} \frac{\mathrm{dN}}{\mathrm{dE}}\mathrm{dE} \tag{4}$$

$$G(10 - 316\,\mathrm{GeV}) = \int_{10\mathrm{GeV}}^{316\mathrm{GeV}} \mathrm{E}\frac{\mathrm{dN}}{\mathrm{dE}}\mathrm{dE} \tag{5}$$

4.4. Source significance and extension

We measured the source significance using a test statistic (TS) defined as Equation 6 , where $\mathcal{L}_1$ corresponds to the likelihood obtained by fitting a model of the source of interest and the background model and $\mathcal{L}_0$ corresponds to the likelihood obtained by fitting the background model only.

$$\mathrm{TS} = 2 \times \log(\mathcal{L}_1/\mathcal{L}_0) \tag{6}$$

In the following, all TS values were calculated using `gtlike` and the corresponding significance was evaluated from the χ^2 distribution with the corresponding number of degrees of freedom (d.o.f.).

We applied two criteria to decide if a source was significantly detected or not. We selected sources with a TS above 16 (3.6 σ with 2 d.o.f) when assuming the TeV morphology. Then, we applied a second filter on this list of sources by requiring TS > 16 at the best GeV shape as well.

To test the extension of each source, following Lande et al. (2012), we defined TS$_{ext}$ as Equation 7 where $\mathcal{L}_{ext}$ represents the likelihood under an extended source hypothesis (5 d.o.f.) and $\mathcal{L}_{ps}$ represents the likelihood assuming a point source (4 d.o.f.). The condition for a source to be extended is TS$_{ext}$ > 16.

$$\mathrm{TS}_{ext} = 2 \times \log(\mathcal{L}_{ext}/\mathcal{L}_{ps}) \tag{7}$$

We also compared the GeV morphology to the TeV shape. The TeV shape was fixed and we fitted only the spectra as a power-law. To assess the significance of the GeV morphology compared to the TeV shape, we computed TS$_{GeV/TeV}$ as Equation 8 where $\mathcal{L}_{TeV}$ corresponds

to the likelihood obtained by fitting the source assuming the TeV shape and $\mathcal{L}_{GeV}$ to the likelihood obtained by fitting the source using the best shape derived using *Fermi*-LAT data.

$$\mathrm{TS}_{GeV/TeV} = 2 \times \log(\mathcal{L}_{GeV}/\mathcal{L}_{TeV}) \tag{8}$$

The correspondence between $\mathrm{TS}_{GeV/TeV}$ and the significance is evaluated from a χ^2 distribution with 2 supplementary d.o.f if the best GeV source is a point-like source and 3 supplementary d.o.f if the best GeV source is an extended source. We considered the GeV morphology to be significantly better than the TeV morphology when the likelihood of the fit is better at more than 3σ level, which means $\mathrm{TS}_{GeV/TeV} > 12$ for a point-like source in GeV, or $\mathrm{TS}_{GeV/TeV} > 14$ for an extended source (uniform disk) in GeV. All values of TS, TS_{ext} and $\mathrm{TS}_{GeV/TeV}$ quoted in the following are obtained using `gtlike`.

4.5.   Procedure followed

The 56 regions summarized in Table 1 were all analyzed using the same procedure with both `gtlike` and `pointlike`:

1. We fitted each source assuming its TeV shape summarized in Table 1. Here, we fixed the position and morphology and fit the spectrum assuming a pure power-law leading the TS to follow a χ^2 distribution with only 2 d.o.f.

   - For sources with significance above 3.6 σ (TS >16 with 2 d.o.f.) we applied steps 2 and 3.
   - For sources with TS < 16 we derived a 99 % upper limit on the flux assuming the TeV morphology and a power–law index of 2.

2. We fitted the source assuming a point source localized with `pointlike` as well as the neighbouring sources within 2°.

3. We fitted the source assuming a disk shape derived using `pointlike` and compared this hypothesis to the point source hypothesis.

To take into account the modifications lead by our analysis and have a consistent analysis between all the regions studied, we performed a third iteration where we fixed the shape of the sources further than 2° of the source of interest but included in our region to the best morphology found in this analysis (see section 5.1).

For the significant sources (TS_{TeV} >16 and TS_{GeV} >16) we derived both the photon and energy fluxes inferred by the fit with the 1 sigma statistical errors, assuming the best morphology. When the source was not significant (TS_{TeV} <16 or TS_{GeV} <16), we derived a 99 % Confidence Level (C.L.) Bayesian upper limit on the flux using a pure power-law model with an index fixed at 2, assuming the TeV shape.

Fermi-LAT spectral points were obtained by splitting the 10–316 GeV range into 3 logarithmically spaced energy bins. A 99 % C.L. upper limit is computed when TS <10 using the approach used by Nolan et al. (2012). The errors on the spectral points represent the statistical errors.

4.6. Systematics on the extension

Two main systematic uncertainties can affect the extension fit of the sources: uncertainties in our model of the galactic diffuse emission and uncertainties on our knowledge of the LAT PSF.

To estimate the systematics due to the uncertainty in our knowledge of the PSF, we used the pre-flight Monte Carlo representation of the PSF. Indeed, before launch, the LAT PSF was determined by detector simulations which we verified in accelerator beam tests (Atwood et al. 2009). However, in-flight data revealed a discrepancy above 3 GeV in the PSF compared to the angular distribution of photons. To account for this uncertainty, we refit our extended source candidates using the pre-flight PSF and consider the difference in extension found using the two PSFs as a systematic error on the extension of a source. This procedure was already used by Lande et al. (2012).

To estimate the uncertainties on the galactic diffuse emission, we used a GALPROP-based model and considered the various components of the diffuse emission model separately. We then individually fit the normalizations of each of them in our likelihood analysis. These various components are gamma-rays produced by IC emission, gamma-rays produced by interactions of CRs with atomic and ionized interstellar gas, and gamma-rays produced in the interactions of CRs with molecular gas. The model component describing the gamma-ray intensity from interactions with molecular gas is further subdivided into seven ranges of Galactocentric distance. It is not expected that this diffuse model is superior to the standard LAT model obtained through an all-sky fit. However, adding degrees of freedom to the background model can remove likely spurious sources that correlate with features in the Galactic diffuse emission. Therefore, this tests systematics that may be due to imperfect modeling of the diffuse emission in the region. This procedure was also used by Lande et al.

(2012).

The total systematic error on the extension of a source was obtained by adding the two errors in quadrature.

4.7. Systematics on the spectral parameters

Three main systematic uncertainties can affect the LAT flux estimate for an extended source: uncertainties in the Galactic diffuse background, uncertainties on the effective area and uncertainties on the shape of the source.

The dominant uncertainty comes from the Galactic diffuse emission and was estimated by using the GALPROP-based model described in Section 4.6.

The second systematic was determined by using modified IRFs whose effective areas bracket the nominal ones. These bracketing IRFs are defined by envelopes above and below the nominal energy dependence of the effective area by linearly connecting differences of (10%, 5%, 20%) at log10(E/MeV) of (2, 2.75, 4), respectively.

The imperfect knowledge of the true γ-ray morphology introduces a last source of error. We derived an estimate of the uncertainty on the shape of the source by using the best model obtained by TeV experiments and compared it to the best extension value obtained in this analysis. We did not compute this component for the sources where the GeV emission is clearly associated to a contamination by the pulsar.

We combined these various errors in quadrature to obtain our best estimate of the total systematic uncertainty at each energy and propagated through to the fit model parameters.

5. Results

Using the procedure described above, we detected 30 sources among the 56 PWNe candidates selected. For each of these detected sources, as explained in Section 4.4, we determined the best morphology by comparing the likelihood of our fit obtained under three different hypotheses: TeV shape, point-like source and extended source. The results of the spatial analysis are shown in Table 4, the last column summarizing the best shape found for each source. Once the best morphology found, we performed a spectral analysis whose results are reported in Tables 6 and 7, while upper limits on non-detections are presented in Tables 8 and 9.

5.1. Extended sources detected above 10 GeV

Most sources are better described using the TeV morphology as a template. This is partly due to the 2 (3 for an extended source) additional degrees of freedom to take into account but also to the low statistics above 10 GeV. Indeed, these sources have on average a low TS value or, are at the limit of our extension threshold, such as HESS J1514-591.

Interestingly, 11 sources are better described using the morphology obtained at GeV energies using the LAT data, 5 of them being extended. Table 5 summarizes the spatial fits in such a case. The results presented here are consistent with Tables 3 and 4 of Lande et al. (2012). One can note that the agreement for HESS J1632−478 is not excellent. The difference in extension (0.35 ±0.06 vs 0.45 ± 0.04 in our analysis) certainly comes from the 3 additional 2FGL sources (2FGL J1631.7−4720c, 2FGL J1630.2−4752 and 2FGL J1632.4−4820c) in the model used by Lande et al. (2012). These sources were below our TS >25 threshold to add a source, and being unidentified, we found no physical reason to add them as we did in the case of PSR J1838-0536.

HESS J1303−631 is a new extended source detected at GeV energies. However, Figure 2 shows that the *Fermi*-LAT excess observed for this source is likely due to 2 point-like sources (one associated with HESS J1303−631 and one associated with Kes 17 (Wu et al. 2011)) but the limited statistics at high energy does not allow us to separate them. When the region is fitted assuming the TeV morphology for HESS J1303−631 and a separate source for Kes 17, the latter hardly reaches TS > 20 and is thus too faint to be added to our model. Nevertheless, the difference between the true spectrum and the spectrum derived in this work will be included in the systematics on the flux taking into account the fact that we do not know the true morphology of the source.

5.2. Pulsars detected above 10 GeV

Only six sources are better described by a point-source model above 10 GeV than with a uniform disk or by the TeV template reported in Table 1: HESS J1708−443, MGRO J0632+17, MGRO J1908+06, MGRO J2019+37, MGRO J2228+61 and VER J0006+727. It is not a surprise to see in Figure 4 and Table 6 that these sources have a rather soft spectrum in comparison to the average index of TeV detected sources and that they are all coincident with bright gamma-ray pulsars. As can be seen on Figures 5, the spectrum obtained above 10 GeV for these sources is in good agreement with the spectrum derived in the 2FGL Catalog released by the Fermi collaboration (Nolan et al. 2012). The γ-ray emission detected by the LAT above 10 GeV is therefore very likely due to the pulsar itself

than to its associated PWN.

Three other sources are coincident with bright Fermi pulsars and present a very soft spectrum in agreement with the 2FGL Catalog as well: HESS J1418-609, MGRO J1958+2848 and MGRO J2031+41. Again, the gamma-ray signal is very likely due to magnetospheric emission and the fact that these sources are rather faint above 10 GeV can explain why the improvement obtained using a point-source model is not significant in comparison to the simple TeV morphology.

To study the contamination of these pulsars to our sources of interest, we used the procedure described in Section 4 but including the pulsars in our models of the regions. The spectra of *Fermi*-LAT pulsars are well characterized by exponentially cutoff power laws with photon indices near 1.5 and cutoff energies between 0.5 and 6 GeV **cite 2PC**. As we selected the data above 10 GeV, we cannot fit the spectral parameters of theses pulsars. Thus we included them in our model assuming the fixed photon index, cutoff energy and normalization extracted from the 2FGL Catalog. It should be noted that some pulsars may deviate from the simple exponential cutoff power law above 10 GeV. This has been proposed for instance for the famous case of the Crab pulsar (citer les papiers Veritas et Magic). In such cases, our fit could still be contaminated by the pulsar, especially in the first energy interval (between 10 and 31.6 GeV).

Table 10 and Figures 5, 6 & 7 show the results of this new fit using the conventions presented in Table 2. As expected for the six point-like sources presented in Figure 5, the low energy part of the spectrum tends to disappear confirming that we only detected a pulsar emission. In the case of MGRO J1908+06, the detection is not significant anymore. To present conservative results, we derived the upper limits assuming the TeV shape of the source.

Figures 6 & 7 show the same behavior for HESS J1418-609 confirming that the signal observed was dominated by the pulsar emission. In the case of HESS J1420-607 and HESS J1119-614, the spectra are now slightly harder but still in very good agreement with the previous ones, which is a good indication that we are seeing the emission from the PWNe and not from their associated pulsars.

5.3. Detections of PWNe candidates

In this section we will describe the new PWNe candidates found in this analysis. We chose them by looking for signal connecting to the TeV spectrum and showing an hard spectrum. HESS J1420-607, HESS J1303-631, HESS J1356-645 & HESS J1119-614 were

already proposed as PWNe by analyses at other wave-length. The detection of these sources by the *Fermi*-LAT tends to confirm this hypothesis.

HESS J1848-018, is classified as UNID. The detection presented in Table 6 show a faint source with a soft spectrum. We will discuss this source in a PWN scenario.

HESS J1420−607

The complex of compact and extended radio/X-ray sources, called Kookaburra (Roberts et al. 1999), spans over about one square degree along the Galactic plane. It has been extensively studied to explain the EGRET source: 3EG J1420−6038/GeV J1417−6100 (Hartman et al. 1999). Within the North-East excess of this complex, labeled 'K3', was discovered the pulsar PSR J1420−6048, a young and energetic pulsar with period 68 ms, characteristic of 13 kyr, and spin down energy of 10^{37} erg s^{-1} (D'Amico et al. 2001). Following X-ray observations by ASCA and later by *Chandra* and *XMM-Newton* revealed an extended X-ray emission around this pulsar identified as a potential PWN (Roberts et al. 2001; Ng et al. 2005). In the South-West side of the large Kookaburra complex lies a bright nebula exhibiting an extended hard X-ray emission, G313.1+0.1, called the 'Rabbit' (Roberts et al. 1999). This X-ray excess was also proposed as a plausible PWN contributing also to the gamma-ray emission detected by EGRET.

In the TeV energy range, the survey of the Galactic plane by H.E.S.S. revealed two very high energy sources in this region: HESS J1420−607 and HESS J1418−609 (Aharonian et al. 2006a). HESS J1420-607 is centered North of PSR J1420−6048 (nearby the K3 nebula), while HESS J1418-609 is coincident with the Rabbit nebula. More recently, *Fermi*-LAT detected pulsed gamma-ray emission from PSR J1420−6048 and PSR J1418−6058, a new gamma-ray pulsar found through blind frequency searches. This new pulsar is coincident with an X-ray source in the Rabbit PWN and has a spin-down power high enough to power the TeV PWN candidate HESS J1418−609.

In our analysis, HESS J1420−607 is detected with a TS of 41 which corresponds to a significance of $\sim 6\sigma$. With a TS of 41.2, the point source hypothesis does not significantly improve the likelihood of our fit in comparison to the TeV morphology (Gaussian of 0.06°) presented in (Aharonian et al. 2006a). Thus assuming the TeV shape, we found an integrated flux F(10-316 GeV)=$(3.2 \pm 0.9_{stat} \pm 1.2_{syst}) \times 10^{-10}$ ph cm^{-2} s^{-1}, a spectral index of $\Gamma = 1.91 \pm 0.27_{stat} \pm 0.30_{syst}$ and an energy flux of E(10-316 GeV) = $(23.1 \pm 6.7_{stat} \pm 9.5_{syst}) \times 10^{-12}$ erg cm^{-2} s^{-1}.

In a second step, following the procedure presented in Section 5.2, we refitted the

spectrum of HESS J1420−607 including PSR J1420−6048 in our model and fixing its spectral parameters found in the 2FGL Catalog. The fit of HESS J1420-607 leads to a lower significance of 5.6σ (TS=35.8, 2 d.o.f) with an integrated flux of F(10-316 GeV)= $(3.4 \pm 0.9_{stat} \pm xx_{syst}) \times 10^{-10}$ ph cm^{-2} s^{-1} and an index of $\Gamma = 1.80 \pm 0.29_{stat} \pm xx_{syst}$.

The connection between the GeV flux as observed by Fermi and the TeV flux as seen by H.E.S.S., visible in Figure 8(a), supports a common origin for the gamma-ray emission. The two black curves present the leptonic and hadronic models proposed by Van Etten & Romani (2010). As said above, the lower energy part of our analysis could still be contaminated by the pulsar even when the 2FGL source associated with the pulsar is added. Therefore, the first energy bin should be taken as an upper limit. This implies that, with the current statistics, all models reproduce reasonably well the GeV and TeV data. A future *Fermi*-LAT off-pulse analysis of this pulsar performed with more statistics could help discriminate between both models.

<h3 style="text-align:center">HESS J1356−645</h3>

HESS J1356−645 is a source detected in the TeV energy range by H.E.S.S. during the continuation of the Galactic Plane Survey (Abramowski et al. 2011c). This extended source lies close to the pulsar PSR J1357−6429 which was discovered during the Parkes multibeam survey of the Galactic Plane (Camilo et al. 2004). Its high spin-down power of $\dot{E} = 3.1 \times 10^{36}$ erg s^{-1} makes it a good candidate to power a PWN. Archival radio and analysis of X-ray data from *ROSAT/PSPC* and *XMM/Newton* have revealed a faint extended structure coincident with the VHE emission (Abramowski et al. 2011c) thus providing another argument in favor of the PWN scenario. In parallel, Lemoine-Goumard et al. (2011) announced the detection of a pulsed signal from PSR J1357−6429 in the γ-ray and X-ray energy ranges using *Fermi*-LAT and *XMM-Newton* data. However, using 29 months of LAT data between 0.1 and 100 GeV, no counterpart to the TeV emission was found in the off pulse window of the pulsar.

The 16 additional months of observations by *Fermi*-LAT between 10 and 316 GeV included in our dataset now enables the detection of a faint counterpart to the TeV emission with a TS = 25.8 (4.7 σ assuming 2 d.o.f.). Since the best GeV morphology does not improve the fit significantly, we used the TeV Gaussian of 0.17° (Abramowski et al. 2011c) for the spectral analysis and derived an integrated flux of F(10-316 GeV)=$(1.2 \pm 0.5_{stat} \pm 0.7_{syst}) \times 10^{-10}$ ph cm^{-2} s^{-1}, an energy flux of E(10-316 GeV)=$(16.8 \pm 6.9 \pm 8.1) \times 10^{-12}$ erg cm^{-2} s^{-1} and a hard spectral index of $\Gamma = 1.01 \pm 0.38 \pm 0.25$.

It should also be noted that, with its low energy cutoff at around 800 MeV in the

Fermi-LAT energy range (Lemoine-Goumard et al. 2011), PSR J1357−6429 is not significant anymore in the 10 to 316 GeV energy range. Therefore, we do not expect to see any changes in the spectral parameters when adding PSR J1357−6429 to the model of the region. This is verified in Table 10 as well as in Figure 9.

The combined GeV-TeV data as seen in Figure 9 provide new constraints concerning the spectral shape of the gamma-ray emission. It is clearly visible in this Figure that the Fermi-LAT spectral points nicely match the H.E.S.S. ones, proving that the GeV and the TeV emission have a common origin. Assuming that the gamma-ray signal is coming from the PWN powered by PSR J1357−6429, Abramowski et al. (2011c) proposed a leptonic scenario (black curve) which provides an excellent fit of the new multi-wavelength data. This model assumes a rather low magnetic field of $\sim 3\mu$G similar to the value observed in other relic PWNe.

HESS J1119−614

During the Parkes multibeam pulsar survey, Camilo et al. (2000) discovered PSR J1119−6127, a young ($\tau = 1.6$ kyr) pulsar with a high $\dot{E} = 2.3 \times 10^{36}$ erg s^{-1} within the supernova remnant G292.2−0.5. Using Chandra observations, Gonzalez & Safi-Harb (2003) and Safi-Harb & Kumar (2008) revealed the presence of a faint and compact PWN close to this pulsar. More recently, a TeV gamma-ray source coincident with PSR J1119−6127 and G292.2−0.5 was announced[3].

Using the method described above, a faint signal consistent with the location of the composite SNR G292.2−0.5 is detected with a TS of 27.3 (4.9 σ with 2 d.o.f.). Since the best GeV morphology does not improve the fit significantly, we used the TeV Gaussian of 0.05° for the spectral analysis and derived an integrated flux of F(10 - 316 GeV) = $(2.1 \pm 0.6_{stat} \pm 1.1_{syst}) \times 10^{-10}$ ph cm^{-2} s^{-1}, an energy flux of E(10-316 GeV) = $(10.4 \pm 3.9_{stat} \pm 4.9_{syst}) \times 10^{-10}$ erg cm^{-2} s^{-1} and a soft index of $\Gamma = 2.15 \pm 0.35_{stat} \pm 0.20_{syst}$.

Nevertheless, as can be seen on Figure 10 and in Table 10, these parameters are contaminated by a low energy component associated to PSR J1119−6127. Once the source 2FGL J1118.8−6128, associated with PSR J1119−6127, included in our model of the region, this contamination decreases and the significance of our GeV source is now just above the detection threshold that we fixed in Section XX, with TS = 16 (3.6 σ with 2 d.o.f.). As can be seen in Figure 10, the low energy point of the SED is now an upper

---

[3]http://cxc.harvard.edu/cdo/snr09/pres/DjannatiAtai_Arache_v2.pdf

442 limit. The best fit parameters in this hypothesis are an integrated flux of F(10-316 GeV) =
443 $(1.5\pm0.6_{stat}\pm XX_{syst})\times10^{-10}$ ph cm^{-2} s^{-1} and an harder index of $\Gamma = 1.80\pm0.48_{stat}\pm XX_{syst}$.
444 To be conservative, we used this fit to derive the physical properties of HESS J1119−614.

445 **TO BE DONE**

446 *HESS J1303−631*

447 HESS J1303−631 was serendipitously discovered in 2004 (Aharonian et al. 2005c) dur-
448 ing an observation campaign for the pulsar binary system PSR B1259−63. It was originally
449 classified as a "dark" accelerator due to the lack of detected counterparts in radio and X-rays
450 with *Chandra* (Mukherjee & Halpern 2005). At this time, a search in the field of view only
451 yielded one plausible counterpart located in the North-Western edge of HESS J1303−631,
452 the high spin-down power pulsar PSR J1301−6305 ($\dot{E} = 1.70 \times 10^{3}6$ erg s^{-1}). The recent
453 detection of a very weak X-ray PWN using *XMM-Newton* observations now allows the solid
454 identification of this source as a VHE PWN associated to the pulsar PSR J1301−6305, lead-
455 ing de Naurois (2011) to classify the TeV excess as an older PWN with a complex morphology
456 and an important offset between the pulsar and nebula.

457 Figures 1 & 3 obtained by Wu et al. (2011) show no significant emission coming from
458 the location of HESS J1303−631 using XX months of *Fermi*-LAT data between 1 and 20
459 GeV. With 16 months of additional data and a higher energy threshold, our analysis now
460 provides a first detection of GeV emission coincident with the TeV source. Nevertheless as
461 discussed in Section 5.1, Figure 2 shows that the detected emission might be contaminated
462 by the source associated to Kes 17. When added to the model as an independent source,
463 Kes 17 hardly reaches a TS of 20 which is lower than our threshold of 25 to add a source.
464 Furthermore, Kes 17 is not included in the Hard Source List. Since we cannot separate these
465 two sources with the current statistics, we decided to take into account this effect of source
466 confusion in our systematics on HESS J1303−631.

467 Assuming our best GeV morphology represented by a Disk shape of 0.5° (see Table 4),
468 we obtained an integrated flux of F(10-316 GeV)=$(5.9 \pm 1.1_{stat} \pm 2.8_{syst}) \times 10^{-10}$ ph cm^{-2}
469 s^{-1}, an energy flux of E(10-316 GeV)= $(43.5 \pm 10.0_{stat} \pm 14.2_{syst}) \times 10^{-12}$ erg cm^{-2} s^{-1} and
470 an index of $\Gamma = 1.71 \pm 0.19_{stat} \pm 0.28_{syst}$. This hard index is in the range of values obtained
471 for PWNe as seen with *Fermi* and is inconsistent with the spectral index of ~ 2.4 derived
472 by Wu et al. (2011) for Kes 17. This is a good evidence that the GeV emission is dominated
473 by the PWN candidate. As can be seen in Fig XX (**modeling**), even though the connection
474 between the GeV and the TeV energy range is not perfect, there is little to doubt that we

have detected a counterpart to the TeV signal. A future analysis with more statistics would greatly help to separate the different components and conclude on the exact spectrum of HESS J1303−631.

<div align="center"><i>HESS J1841−055</i></div>

HESS J1841−055 was discovered during the H.E.S.S. Galactic Plane Survey (Aharonian et al. 2008b) and remained an UNID source since then. The emission is highly extended and show possibly three peaks suggesting that the TeV emission is composed of more than one source. Using *INTEGRAL* data, Sguera et al. (2009) proposed the high-mass X-ray binary HMXB system AX J1841.0−0536 as a potential counterpart, at least for a part of the emission. Tibolla (2011) proposed the association of HESS J1841−055 to an ancient PWN powered by PSR J1841−0524, PSR J1838−0549 or both as each pulsar taken independently would need an efficiency greater than 100% to power a potential PWN associated to the TeV source. More recently, the blind search detection of the new gamma-ray pulsar PSR J1838−0537 with *Fermi*-LAT provided another good counterpart of the TeV source. Indeed, assuming a distance of 2 kpc, Pletsch et al. (2012) estimated that PSR J1838−0537 is sufficiently energetic to power the whole TeV source with a conversion efficiency of 0.5%, similar to other suggested pulsar/PWN associations (Hessels et al. 2008).

HESS J1841−055 is detected as a significantly extended source with our analysis (TS_{ext}= 38.3) at a position consistent with the TeV source but with a slightly larger extension (0.57 ° with respect to 0.41 ° × 0.25 ° for the TeV source). However, the GeV best morphology does not significantly improve the fit compared to the TeV morphology ($\text{TS}_{GeV/TeV}$= 13.0, 2.8σ with 3 d.o.f.). Thus assuming the TeV shape, our best fit yielded an integrated flux of F(10-316 GeV) = $(9.3 \pm 1.9_{stat} \pm 3.9_{syst}) \times 10^{-10}$ for an energy flux of G(10-316 GeV) = $(79.6 \pm 16.0_{stat} \pm 19.1_{syst}) \times 10^{-12}$ erg cm^{-2} s^{-1} and a hard index of $\Gamma = 1.56 \pm 0.20_{stat} \pm 0.32_{syst}$ consistent with the average value for PWNe detected by the *Fermi*-LAT.

As can be seen in Figure 12, the *Fermi*-LAT spectral points nicely match the H.E.S.S. ones, suggesting a common origin. The hard *Fermi*-LAT spectrum detected imply that a curvature must arise between the TeV energy range and the GeV energy range. This is typical of most PWNe detected by *Fermi* and HESS which present an inverse-Compton emission peaking at few hundreds of GeV and would favor the PWN scenario. However, as said above, this source is extremely extended in both wavelengths and could be composed of several gamma-ray sources. Follow-up observations with HESS and *Fermi* would be needed to unveil the real nature of HESS J1841−055.

HESS J1848-018

HESS J1848-018 *(WR121a, W43, TeV J1848-017).*

5.4. Constraints obtained from non-detections

This section will present the sources for which the emission was not significant but for which the upper limit show an interesting behavior to bring new constraints on the models.

HESS J1026−582

HESS J1026−582 was discovered during a new analysis of the region of HESS J1023−577 (Abramowski et al. 2011d). The presence of PSR J1028−5819, detected by the Parkes Radio telescope Keith et al. (2008), close to the TeV emission suggested a PWN scenario to explain this VHE source. This hypothesis is consolidated by the spin-down power energy of PSR J1028−5819, $\dot{E} = 8.43 \times 10^{35}$ erg s^{-1} (Abdo et al. 2009a), which is high enough to power a PWN.

No significant GeV emission coming from the location of the TeV excess was detected in our analysis. The very low TS value derived (see Tables 8 & 9) give few hope for a future detection of this source in this energy range on a short time scale. The upper limits presented on Figure ??how that a curvature is needed between the TeV and the GeV energy range. This suggests an inverse-Compton peak consistent with a PWN hypothesis.

HESS J1458−608

PSR J1459−60 (Abdo et al. 2010e) is an energetic pulsar with an $\dot{E} = 9.2 \times 10^{35}$ erg s^{-1} sufficient to power a PWN. A potential PWN, HESS J1458−608, was discovered 9.6′ from PSR J1459−60 using H.E.S.S. data after a dedicated observation de los Reyes et al. (2012) based on a marginal detection in the 2004 Galactic Plane Survey.

The source was not significantly detected in our analysis above 10 GeV (TS = 12.3). It can also be noted from Table 9 that the marginal emission detected comes from the low energy range studied and is more likely associated to PSR J1459−60. Figure 6(d) shows that even taking into account the pulsar in our model of the region, the SED is still contaminated at low energy. Nevertheless, the upper limits of the two high energy bins show that a change

in the slope of the spectrum is needed between the TeV and the GeV component.

TO BE DONE

HESS J1626−490

HESS J1626−490 is another unidentified source detected during the H.E.S.S. Galactic Plane Survey (Aharonian et al. 2008b). EGER (2011) found no X-Ray source fulfilling the energetic requirement to explain the TeV emission using *XMM-Newton* observations. However, the author suggested that a hadronic scenario based on the interaction of the SNR G335.2+00.1 with a ^{12}CO molecular cloud could explain the TeV emission.

Figure XX shows that the upper limits derived following the procedure described in Section 4 require a change in the slope of the spectrum, consistent with the model presented in Figure 4 of EGER (2011).

HESS J1813−178

HESS J1813-178 was discovered during the H.E.S.S. Survey of the Inner Galaxy (Aharonian et al. 2005a). It remained unidentified until the discovery of the SNR G12.8-0.0 Brogan et al. (2005). X-ray studies resolved the emission into a point-like source and an extended nebula Funk et al. (2007). The discovery of PSR J1813−1749 Gotthelf & Halpern (2009) confirmed a PWN/SNR scenario. With its $\dot{E} = 5.6 \times 10^{37}$ erg s^{-1} (Halpern et al. 2012), this pulsar is the third most energetic pulsar of the Galaxy. Thus it could produce a PWN observable in TeV/GeV range.

Funk et al. (2007) & Fang & Zhang (2010) preferred a leptonic scenario to explain the GeV/TeV emission to a potential hadronic scenario. The upper limits derived using the procedure described in sect. 4. show that the spectrum of HESS J1813−178 cannot be flat between the TeV and the GeV energy ranges and suggest peak with an energy cutoff located between the two energy ranges. Therefore, this suggests a PWN scenario as determined in previous works.

TO BE DONE

5.5. Conclusion

To be done later....

6. Discussion

6.1. PWNe

---

[4]http://healpix.jpl.nasa.gov/

REFERENCES

Abdo, A. A., et al. 2007a, ApJ, 658, L33

—. 2007b, ApJ, 664, L91

—. 2009a, ApJ, 695, L72

—. 2009b, Phys. Rev. D, 80, 122004

—. 2009c, ApJ, 696, 1084

—. 2009d, ApJ, 700, L127

—. 2010a, ApJS, 188, 405

—. 2010b, ApJ, 708, 1254

—. 2010c, ApJ, 713, 146

—. 2010d, ApJ, 722, 1303

—. 2010e, ApJS, 187, 460

Abramowski, A., et al. 2011a, A&A, 531, A81

—. 2011b, A&A, 528, A143

—. 2011c, A&A, 533, A103

—. 2011d, A&A, 525, A46

—. 2012, ArXiv e-prints

Acciari, V. A., et al. 2010, ApJ, 719, L69

Acero, F., Djannati-Ataï, A., Förster, A., Gallant, Y., Renaud, M., & for the H. E. S. S. collaboration. 2012, ArXiv e-prints

Acero, F., et al. 2011, A&A, 525, A45

Ackermann, M., et al. 2011, ApJ, 726, 35

Aharonian, F., et al. 2005a, Science, 307, 1938

—. 2005b, A&A, 435, L17

604   —. 2005c, A&A, 439, 1013

605   —. 2006a, A&A, 456, 245

606   —. 2006b, A&A, 460, 365

607   —. 2006c, A&A, 457, 899

608   —. 2006d, ApJ, 636, 777

609   —. 2007, A&A, 472, 489

610   —. 2008a, A&A, 484, 435

611   —. 2008b, A&A, 477, 353

612   —. 2009, A&A, 499, 723

613   Aleksić, J., et al. 2012, Astroparticle Physics, 35, 435

614   Aliu, E. e. a. 2011, ArXiv e-prints

615   Atwood, W. B., et al. 2009, ApJ, 697, 1071

616   Bartoli, B., et al. 2012, ApJ, 745, L22

617   Brogan, C. L., Gaensler, B. M., Gelfand, J. D., Lazendic, J. S., Lazio, T. J. W., Kassim,
618   N. E., & McClure-Griffiths, N. M. 2005, ApJ, 629, L105

619   Brun, F., de Naurois, M., Hofmann, W., Carrigan, S., Djannati-Ataï, A., Ohm, S., & for the
620   H. E. S. S. Collaboration. 2011, ArXiv e-prints

621   Buehler, R., et al. 2012, ApJ, 749, 26

622   Camilo, F., Kaspi, V. M., Lyne, A. G., Manchester, R. N., Bell, J. F., D'Amico, N., McKay,
623   N. P. F., & Crawford, F. 2000, ApJ, 541, 367

624   Camilo, F., et al. 2004, ApJ, 611, L25

625   Chaves, R. C. G., Renaud, M., Lemoine-Goumard, M., & Goret, P. 2008, in American Insti-
626   tute of Physics Conference Series, Vol. 1085, American Institute of Physics Conference
627   Series, ed. F. A. Aharonian, W. Hofmann, & F. Rieger, 372–375

628   D'Amico, N., et al. 2001, ApJ, 552, L45

de Jager, O. C., & Djannati-Ataï, A. 2009, in Astrophysics and Space Science Library, Vol. 357, Astrophysics and Space Science Library, ed. W. Becker, 451

de Jager, O. C., et al. 2009, ArXiv e-prints

de los Reyes, R., Zajczyk, A., Chaves, R. C. G., & for the H. E. S. S. collaboration. 2012, ArXiv e-prints

de Naurois, M. 2011, ArXiv e-prints

Djannati-Ataĭ, A., de Jager, O. C., Terrier, R., & et al. 2008, in International Cosmic Ray Conference, Vol. 2, International Cosmic Ray Conference, 823–826

EGER, P. 2011, in International Cosmic Ray Conference, Vol. 7, International Cosmic Ray Conference, 44

Esposito, P., Tiengo, A., de Luca, A., & Mattana, F. 2007, A&A, 467, L45

Fang, J., & Zhang, L. 2010, ApJ, 718, 467

Funk, S., et al. 2007, A&A, 470, 249

Gonzalez, M., & Safi-Harb, S. 2003, ApJ, 591, L143

Górski, K. M., Hivon, E., Banday, A. J., Wandelt, B. D., Hansen, F. K., Reinecke, M., & Bartelmann, M. 2005, ApJ, 622, 759

Gotthelf, E. V., & Halpern, J. P. 2009, ApJ, 700, L158

Grondin, M.-H., et al. 2011, ApJ, 738, 42

Hall, T. A., et al. 2003, ApJ, 583, 853

Halpern, J. P., Gotthelf, E. V., & Camilo, F. 2012, ApJ, 753, L14

Hartman, R. C., et al. 1999, ApJS, 123, 79

Hessels, J. W. T., et al. 2008, ApJ, 682, L41

Hofverberg, P., Chaves, R. C. G., Méhault, J., de Naurois, M., & for the H. E. S. S. Collaboration. 2011, ArXiv e-prints

Hoppe, S. 2008, in International Cosmic Ray Conference, Vol. 2, International Cosmic Ray Conference, 579–582

James, F., & Roos, M. 1975, Comput. Phys. Commun.

Keith, M. J., Johnston, S., Kramer, M., Weltevrede, P., Watters, K. P., & Stappers, B. W. 2008, MNRAS, 389, 1881

Kerr, M. 2011, ArXiv e-prints

Lande, J., et al. 2012, ArXiv e-prints

Lemiere, A., Slane, P., Gaensler, B. M., & Murray, S. 2009, ApJ, 706, 1269

Lemoine-Goumard, M., et al. 2011, A&A, 533, A102

Mattox, J. R., et al. 1996, ApJ, 461, 396

McArthur, S. e. a. 2011, ArXiv e-prints

Mukherjee, R., & Halpern, J. P. 2005, ApJ, 629, 1017

Ng, C.-Y., Roberts, M. S. E., & Romani, R. W. 2005, ApJ, 627, 904

Nolan, P. L., et al. 2012, ApJS, 199, 31

Pletsch, H. J., et al. 2012, ApJ, 755, L20

Renaud, M., Goret, P., & Chaves, R. C. G. 2008, in American Institute of Physics Conference Series, Vol. 1085, American Institute of Physics Conference Series, ed. F. A. Aharonian, W. Hofmann, & F. Rieger, 281–284

Roberts, M. S. E., Romani, R. W., & Johnston, S. 2001, ApJ, 561, L187

Roberts, M. S. E., Romani, R. W., Johnston, S., & Green, A. J. 1999, ApJ, 515, 712

Rousseau, R., Grondin, M.-H., Van Etten, A., Lemoine-Goumard, M., Bogdanov, S., Hessels, J., & Kaspi, V. 2012, å

Safi-Harb, S., & Kumar, H. S. 2008, ApJ, 684, 532

Sguera, V., Romero, G. E., Bazzano, A., Masetti, N., Bird, A. J., & Bassani, L. 2009, ApJ, 697, 1194

Sheidaei, F., Djannati-Ataï, A., Gast, H., & for the HESS Collaboration. 2011, ArXiv e-prints

Slane, P., Castro, D., Funk, S., Uchiyama, Y., Lemiere, A., Gelfand, J. D., & Lemoine-Goumard, M. 2010, ApJ, 720, 266

Tam, P. H. T., Wagner, S. J., Tibolla, O., & Chaves, R. C. G. 2010, A&A, 518, A8

Terrier, R., Mattana, F., Djannati-Atai, A., Marandon, V., Renaud, M., & Dubois, F. 2008, in American Institute of Physics Conference Series, Vol. 1085, American Institute of Physics Conference Series, ed. F. A. Aharonian, W. Hofmann, & F. Rieger, 312–315

Tibolla, O. 2011, in International Cosmic Ray Conference, Vol. 6, International Cosmic Ray Conference, 197

Uchiyama, Y. 2011, ArXiv e-prints

Van Etten, A., & Romani, R. W. 2010, ApJ, 711, 1168

Weekes, T. C., et al. 2002, Astroparticle Physics, 17, 221

Wu, J. H. K., Wu, E. M. H., Hui, C. Y., Tam, P. H. T., Huang, R. H. H., Kong, A. K. H., & Cheng, K. S. 2011, ApJ, 740, L12

Zavlin, V. E. 2007, ApJ, 665, L143

Table 1.   List of TeV sources analyzed

TeV source	Type	(l,b) (°)	TeV morphology	Reference
HESS J1018-589	UNID	(284.23,-1.72)	pointsource	(Abramowski et al. 2012)
HESS J1023-577	Massive Star Cluster	(284.22,-0.40)	gaussian(0.18)	(Abramowski et al. 2011d)
HESS J1026-582	PWN	(284.80,-0.52)	gaussian(0.14)	(Abramowski et al. 2011d)
HESS J1119-614	PWN	(292.10,-0.49)	gaussian(0.05)	[5]
HESS J1303-631	PWN	(304.24,-0.36)	gaussian(0.16)	(Aharonian et al. 2005c)
HESS J1356-645	PWN	(309.81,-2.49)	gaussian(0.20)	(Abramowski et al. 2011c)
HESS J1418-609	PWN	(313.25,0.15)	Ell. gaussian(0.08,0.06)	(Aharonian et al. 2006a)
HESS J1420-607	PWN	(313.56,0.27)	gaussian(0.06)	(Aharonian et al. 2006a)
HESS J1427-608	UNID	(314.41,-0.14)	Ell. gaussian(0.04,0.08)	(Aharonian et al. 2008b)
HESS J1458-608	PWN	(317.75, -1.7)	gaussian(0.17)	(de los Reyes et al. 2012)
HESS J1503-582	UNID	(319.62,0.29)	gaussian(0.26)	(Renaud et al. 2008)
HESS J1507-622	UNID	(317.95,-3.49)	gaussian(0.15)	(Acero et al. 2011)
HESS J1514-591	PWN	(320.33,-1.19)	Ell. gaussian(0.11,0.04)	(Aharonian et al. 2005b)
HESS J1554-550	PWN	(327.16,-1.07)	pointsource	(Acero et al. 2012)
HESS J1614-518	massive star cluster	(331.52,-0.58)	Ell. gaussian(0.23,0.15)	(Aharonian et al. 2006d)
HESS J1616-508	PWN	(332.39,-0.14)	gaussian(0.14)	(Aharonian et al. 2006d)
HESS J1626-490	UNID	(334.77,0.05)	Ell. gaussian(0.07,0.10)	(Aharonian et al. 2008b)
HESS J1632-478	PWN	(336.38,0.19)	Ell. gaussian(0.21,0.06)	(Aharonian et al. 2006d)
HESS J1634-472	UNID	(337.11,0.22)	gaussian(0.11)	(Aharonian et al. 2006d)
HESS J1640-465	PWN	(338.32,-0.02)	gaussian(0.04)	(Aharonian et al. 2006d)
HESS J1702-420	UNID	(344.30,-0.18)	Ell. gaussian(0.30,0.15)	(Aharonian et al. 2006d)
HESS J1708-443	PWN	(343.06,-2.38)	gaussian(0.29)	(Abramowski et al. 2011b)
HESS J1718-385	PWN	(348.83,-0.49)	Ell. gaussian(0.15,0.07)	(Aharonian et al. 2007)
HESS J1729-345	UNID	(353.44,-0.13)	gaussian(0.14)	(Abramowski et al. 2011a)
HESS J1804-216	UNID	(8.40,-0.03)	Ell. gaussian(0.16,0.27)	(Aharonian et al. 2006d)
HESS J1809-193	PWN	(11.18,-0.09)	Ell. gaussian(0.53,0.25)	(Aharonian et al. 2007)
HESS J1813-178	PWN	(12.81,-0.03)	gaussian(0.04)	(Aharonian et al. 2006d)
HESS J1818-154	PWN	(15.41,0.17)	gaussian(0.14)	(Hofverberg et al. 2011)
HESS J1825-137	PWN	(17.71,-0.70)	Ell. gaussian(0.13,0.12)	(Aharonian et al. 2006b)
HESS J1831-098	PWN	(21.85,-0.11)	gaussian(0.15)	(Sheidaei et al. 2011)
HESS J1833-105	PWN	(21.51,-0.88)	pointsource	(Djannati-Ataǐ et al. 2008)
HESS J1834-087	UNID	(23.24,-0.31)	gaussian(0.09)	(Aharonian et al. 2006d)
HESS J1837-069	UNID	(25.18,-0.12)	Ell. gaussian(0.12,0.05)	(Aharonian et al. 2006d)
HESS J1841-055	UNID	(26.80,-0.20)	Ell. gaussian(0.41,0.25)	(Aharonian et al. 2008b)
HESS J1843-033	UNID	(29.30,0.51)	pointsource	(Hoppe 2008)
HESS J1846-029	PWN	(29.70,-0.24)	pointsource	(Djannati-Ataǐ et al. 2008)
HESS J1848-018	Massive Star Cluster	(31.00,-0.16)	gaussian(0.32)	(Chaves et al. 2008)
HESS J1849-000	PWN	(32.64,0.53)	pointsource	(Terrier et al. 2008)
HESS J1857+026	UNID	(35.96,-0.06)	Ell. gaussian(0.11,0.08)	(Aharonian et al. 2008b)
HESS J1858+020	UNID	(35.58,-0.58)	Ell. gaussian(0.08,0.02)	(Aharonian et al. 2008b)
HESS J1912+101	PWN	(44.39,-0.07)	gaussian(0.26)	(Aharonian et al. 2008a)
MGRO J0631+105	PWN	(201.30,0.51)	pointsource	(Abdo et al. 2009d)
MGRO J0632+17	PWN	(195.34,3.78)	gaussian(1.30)	(Abdo et al. 2009d)
MGRO J1844-035	UNID	(28.91,-0.02)	pointsource	(Abdo et al. 2009d)
MGRO J1900+039	UNID	(37.42,-0.11)	pointsource	(Abdo et al. 2009d)
MGRO J1908+06	UNID	(40.39,-0.79)	gaussian(0.34)	(Aharonian et al. 2009)

Table 1—Continued

TeV source	Type	(l,b) (°)	TeV morphology	Reference
MGRO J1958+2848	PWN	(65.85,-0.23)	pointsource	(Abdo et al. 2009d)
MGRO J2019+37	PWN	(75.00,0.39)	gaussian(0.55)	(Abdo et al. 2007b)
MGRO J2031+41	UNID	(79.53,0.64)	gaussian(1.50)	(Abdo et al. 2007b)
MGRO J2031+41	UNID	(80.25,1.07)	gaussian(0.10)	(Bartoli et al. 2012)
MGRO J2228+611	PWN	(106.57,2.91)	pointsource	(Abdo et al. 2009d)
VER J0006+727	PWN	(119.58,10.20)	pointsource	(McArthur 2011)
VER J1930+188	PWN	(54.10,0.26)	pointsource	(Acciari et al. 2010)
VER J1959+208	PSR	(59.20,-4.70)	pointsource	(Hall et al. 2003)
VER J2016+372	UNID	(74.94,1.15)	pointsource	(Aliu 2011)
W49A	Star Forming Region	(43.27,-0.00)	pointsource	(Brun et al. 2011)

Note. — The first two columns are TeV source names and types as defined in the TeV catalog provided by the university of Chicago: PWN for Pulsar Wind Nebula, PSR for Pulsars, UNID for Unidentified sources, Massive Star Cluster and Star Forming Regions. The 3rd column reports the Galactic coordinates for each source. The 4th column presents the shape that best describes the source at TeV energies, together with a reference in the 5th column.

Table 2.   List of sources with a pulsar within 0.5°

Source name	Pulsar Name	distance (°)	pulsar 2FGL name	Included in the model
HESS J1018-589	PSR J1016-5857	0.22	2FGL J1016.5-5858	N [a]
HESS J1023-577	PSR J1023-5746	0.05	2FGL J1022.7-5741	N [b]
HESS J1026-5819	PSR J1028-5819	0.27	2FGL J1028.5-5819	Y
HESS J1119-614	PSR J1119-6127	0.07	2FGL J1118.8-6128	N [a]
HESS J1356-645	PSR J1357-6429	0.12	2FGL J1356.0-6436	N [a]
HESS J1418-609	PSR J1418-6058	0.05	2FGL J1418.7-6058	N [b]
HESS J1420-607	PSR J1420-6048	0.05	2FGL J1420.1-6047	N [b]
HESS J1458-608	PSR J1459-6053	0.17	2FGL J1459.4-6054	N [a]
HESS J1514-591	PSR J1513-5908	0.03	-	N [b]
HESS J1702-420	PSR J1702-4128	0.53	–	N [c]
HESS J1708-443	PSR J1709-4429	0.25	2FGL J1709.7-4429	N [b]
HESS J1718-385	PSR J1718-3825	0.13	2FGL J1718.3-3827	N [a]
HESS J1804-216	PSR J1803-2149	0.27	2FGL J1803.3-2148	N [b]
HESS J1833-105	PSR J1833-1034	0.01	2FGL J1833.6-1032	N [a]
MGRO J0631+105	PSR J0631+1036	0.10	2FGL J0631.5+ 1035	N [a]
MGRO J0632+17	PSR J0633+1746	0.00	2FGL J0633.9+1746	N [a]
MGRO J1908+06	PSR J1907+0602	0.23	2FGL J1907.9+0602	N [a]
MGRO J1958+2848	PSR J1958+2846	0.12	2FGL J1958.6+2845	N [a]
MGRO J2019+37	PSR J2021+3651	0.36	2FGL J2021.0+3651	N [b]
MGRO J2228+61	PSR J2229+6114	0.09	2FGL J2229+6114	N [a]
VER J0006+727	PSR J0007+7303	0.26	2FGL J0007.0+7303	N [a]

a- The distance between the pulsar and the source is lower than 0.27°.
b- The pulsar is located inside the edge of the TeV shape.
c- The pulsar shown no significant excess.

Note. — List of sources having a known γ-ray pulsar within 0.5°. The two first column shows the TeV source and the pulsar name. The third column show the distance between the TeV source and the GeV pulsar. The pulsar position comes from **Citer 2PC**. In the fourth colum Y means that we added the pulsar to the model and N that we didn't added it.

Table 3. Locations and spectral parameters of additional background sources above 10 GeV

Source name	Galactic coordinates (°)	TS	Prefactor	Index
2FGL J1504.5–6121	(311.81,0.30)	30.7	$(1.2 \pm 0.4) \times 10^{-15}$	1.8 ± 0.3
2FGL J1836.8–0623c	(25.41,0.42)	25.1	$(9.4 \pm 1.9) \times 10^{-16}$	2.0 ± 0.4
2FGL J1823.1–1338c	(17.51,-0.12)	30.4	$(4.9 \pm 0.5) \times 10^{-15}$	2.9 ± 0.7
PSR J1838–0536	(26.28,0.62)	16.1	$(5.0 \pm 1.8) \times 10^{-17}$	4.1 ± 1.0
Background Source 1	(333.59,-0.31)	29	$(6.5 \pm 2.5) \times 10^{-17}$	4.3 ± 0.9
Background Source 2	(336.96, -0.07)	25.0	$(1.2 \pm 0.4) \times 10^{-15}$	1.9 ± 0.4
Background Source 3	(339.37,-1.18)	29.9	$(1.3 \pm 0.4) \times 10^{-15}$	1.5 ± 0.3

Note. — The first two columns describe the source names and their corresponding Galactic coordinates. The test statistic (TS) for the source significance is provided in the 3rd column. The spectral results are presented in columns 4 and 5 for a power-law model (Equation 2) with a scale parameter $E_0 = 56234$ MeV which corresponds to the middle of the 10–316 GeV interval in log scale. PSR J1838$-$0536 has been added to help the morphology fit of HESS J1841$-$055 which is a diffuse source. The spectral fit is consistent with the pulsar component (index of$\sim$ 5).

Table 4.   Morphological results for LAT-detected TeV sources above 10 GeV

TeV source	TS_{TeV}	TS_{GeV}	TS_{ext}	$\mathrm{TS}_{GeV/TeV}$	Significance	Morphology
HESS J1018-589	29.1	29.1	0	0	0	TeV
HESS J1023-575	52.0	49.4	1.5	-	-	TeV
HESS J1119-614	27.3	27.3	12.2	0	0	TeV
HESS J1303-631	37.2	52.5	24.9	15.3	3.1	Disk
HESS J1356-645	25.8	28.8	2.5	3.0	1.2	TeV
HESS J1418-609	30.4	30.9	0.1	-	-	TeV
HESS J1420-607	41	41.2	1.8	-	-	TeV
HESS J1507-622	20.9	22.1	7.2	-	-	TeV
HESS J1514-591	169.5	147.3	10.4	-	-	TeV
HESS J1614-518	119.6	146.3	59.6	26.7	4.5	Disk
HESS J1616-508	76.2	79.6	19.9	3.4	1.0	TeV
HESS J1632-478	120.8	143	52.4	22.2	4.3	Disk
HESS J1634-472	28.7	29.6	5.2	0.9	0.5	TeV
HESS J1640-465	49	52.9	0	3.9	1.5	TeV
HESS J1708-443	721.8	1153.3	0	431.5		point–like
HESS J1804-216	131	137.8	41.1	6.8	1.8	TeV
HESS J1825-137	55.7	78.1	27.9	22.4	4.0	Disk
HESS J1834-087	31	28.7	2.6	-	-	TeV
HESS J1837-069	74	106.7	45.8	32.7	5.1	Disk
HESS J1841-055	52	65	38.3	13.0	2.8	TeV
HESS J1848-018	18.7	18.6	0	-	-	TeV
HESS J1857+026	52.5	53.1	12.1	-	-	TeV
MGRO J0632+17	698.8	2056.3	2.5	1357.5		point–like
MGRO J1908+06	16.4	37.2	0.2	20.8	4.2	point–like
MGRO J1958+2848	20.8	23.5	0.2	2.7	1.1	TeV
MGRO J2019+37	31.1	98.5	0	61.3	8.0	point–like
MGRO J2031+41	72.1	66.4	2.9	-	-	TeV
MGRO J2228+61	94.5	114	0	19.5	4.0	point–like
VER J0006+727	654.5	1205.6	1.3	551.1		point–like
VER J2016+372	31.4	32.9	0.3	1.5	0.7	TeV

Note. — Results of the morphological analysis for all LAT-detected TeV sources. The fits assumed either the TeV template defined in Table 1, a point-source model or a uniform disk model (see Equation 1). The definition of TS_{TeV}, TS_{GeV}, TS_{ext} and $\mathrm{TS}_{GeV/TeV}$ is reported in Section 4.4. The significance of the extension is measured using the TS_{ext} criterium defined in Section 4.4.

Table 5.   Morphological results for LAT-detected TeV sources for which TS_{GeV} is significantly better than TS_{TeV} above 10 GeV

TeV source	Morphology	TS_{ext}	(l,b) °	extension(°)
HESS J1303-631	Disk	24.9	(304.44, -0.18)	$0.50 \pm 0.05_{stat}$
HESS J1614-518	Disk	59.8	(331.66, -0.66)	$0.42 \pm 0.06_{stat}$
HESS J1632-478	Disk	52.4	(336.38, 0.19)	$0.45 \pm 0.04_{stat}$
HESS J1708-443	point–like	0	(343.11,-2.70)	-
HESS J1825-137	Disk	27.9	(17.56,-0.47)	$0.65 \pm 0.04_{stat}$
HESS J1837-069	Disk	45.8	(25.08,-0.13)	$0.32 \pm 0.05_{stat}$
MGRO J0632+17	point–like	2.5	(195.13, 4.27)	-
MGRO J1908+06	point–like	0.2	(40.39, -0.79)	-
MGRO J2019+37	point–like	0	(75.27, 0.14)	-
MGRO J2228+61	point–like	0	(106.67, 2.93)	-
VER J0006+727	point–like	1.3	(119.69, 10.47)	-

Note. — Results of the morphological analysis for LAT-detected TeV sources better described using the shape fitted at GeV energies. The fits assumed either a point-source model or a uniform disk model (see Equation 1) whose centroid and extension are provided in columns 4 and 5 respectively. The significance of the extension is measured using the TS_{ext} criterium defined in Section 4.4.

Table 6.   Spectral fitting results for LAT-detected TeV sources above 10 GeV

TeV source	TS	F(10–316 GeV) $(10^{-10}$ ph cm^{-2} s^{-1})	E(10–316 GeV) $(10^{-12}$ erg cm^{-2} s^{-1})	Γ
HESS J1018-589	29.1	$1.7 \pm 0.5 \pm 0.4$	$7.0 \pm 3.0 \pm 2.4$	$2.41 \pm 0.49 \pm 0.49$
HESS J1023-575	52	$4.5 \pm 0.9 \pm 2.0$	$24.6 \pm 6.8 \pm 9.4$	$2.04 \pm 0.26 \pm 0.35$
HESS J1119-614	27.3	$2.1 \pm 0.6 \pm 1.1$	$10.4 \pm 3.9 \pm 4.9$	$2.15 \pm 0.35 \pm 0.20$
HESS J1303-631	52.5	$5.9 \pm 1.1 \pm 2.8$	$43.5 \pm 10.0 \pm 14.2$	$1.71 \pm 0.19 \pm 0.28$
HESS J1356-645	25.8	$1.2 \pm 0.5 \pm 0.7$	$16.8 \pm 6.9 \pm 8.1$	$1.01 \pm 0.38 \pm 0.25$
HESS J1418-609	30.4	$4.1 \pm 1.0 \pm 1.0$	$10.7 \pm 3.6 \pm 4.4$	$3.54 \pm 0.81 \pm 0.6$
HESS J1420-607	41	$3.2 \pm 0.9 \pm 1.2$	$23.1 \pm 6.7 \pm 9.5$	$1.91 \pm 0.27 \pm 0.30$
HESS J1507-622	20.9	$1.5 \pm 0.5 \pm 0.5$	$6.7 \pm 3.0 \pm 3.1$	$2.33 \pm 0.48 \pm 0.28$
HESS J1514-591	169.5	$6.4 \pm 0.9 \pm 1.4$	$46.8 \pm 8.5 \pm 8.7$	$1.72 \pm 0.15 \pm 0.14$
HESS J1614-518	146.3	$12.0 \pm 1.0 \pm 3.0$	$79.7 \pm 12.2 \pm 18.4$	$1.85 \pm 0.14 \pm 0.18$
HESS J1616-508	76.2	$9.4 \pm 1.4 \pm 2.3$	$47.1 \pm 9.3 \pm 10.9$	$2.16 \pm 0.19 \pm 0.20$
HESS J1632-478	143.0	$15.3 \pm 1.7 \pm 3.4$	$94.8 \pm 13.8 \pm 24.7$	$1.90 \pm 0.14 \pm 0.23$
HESS J1634-472	28.7	$5.1 \pm 1.2 \pm 2.6$	$30.1 \pm 8.7 \pm 12.0$	$1.97 \pm 0.26 \pm 0.21$
HESS J1640-465	49.03	$4.8 \pm 1.0 \pm 2.1$	$30.3 \pm 7.6 \pm 8.4$	$1.93 \pm 0.24 \pm 0.25$
HESS J1708-443	1153.3	$21.8 \pm 1.5 \pm 3.6$	$51.5 \pm 4.2 \pm 11.1$	$4.09 \pm 0.23 \pm 0.35$
HESS J1804-216	131.0	$13.7 \pm 1.6 \pm 2.7$	$75.2 \pm 12.5 \pm 16.7$	$2.05 \pm 0.16 \pm 0.21$
HESS J1825-137	78.1	$13.4 \pm 2.1 \pm 8.7$	$10.9 \pm 2.0 \pm 5.2$	$1.61 \pm 0.15 \pm 0.39$
HESS J1834-087	31.0	$5.3 \pm 1.2 \pm 1.9$	$25.2 \pm 8.1 \pm 12.1$	$2.23 \pm 0.35 \pm 0.37$
HESS J1837-069	106.7	$10.8 \pm 1.6 \pm 5.0$	$92.6 \pm 18.1 \pm 28.7$	$1.74 \pm 0.14 \pm 0.50$
HESS J1841-055	52.01	$9.3 \pm 1.9 \pm 3.9$	$79.6 \pm 16.0 \pm 19.1$	$1.56 \pm 0.20 \pm 0.32$
HESS J1848-018	18.7	$7.4 \pm 1.9 \pm 3.2$	$30.0 \pm 10.1 \pm 16.5$	$2.46 \pm 0.80 \pm 0.52$
HESS J1857+026	52.5	$3.7 \pm 0.5 \pm 1.6$	$54.0 \pm 6.9 \pm 9.1$	$0.99 \pm 0.25 \pm 0.27$
MGRO J0632+17	2056.3	$25.6 \pm 1.5 \pm 6.7$	$54.5 \pm 3.7 \pm 15.1$	$5.06 \pm 0.26 \pm 0.57$
MGRO J1908+06	37.2	$2.3 \pm 0.7 \pm 1.2$	$26.2 \pm 2.3 \pm 3.4$	$6.17 \pm 1.17 \pm 1.5$
MGRO J1958+2848	20.8	$1.3 \pm 0.4 \pm 0.3$	$3.0 \pm 1.1 \pm 0.8$	$4.36 \pm 1.01 \pm 1.00$
MGRO J2019+37	98.5	$3.4 \pm 0.7 \pm 1.1$	$7.1 \pm 1.6 \pm 1.9$	$5.33 \pm 1.01 \pm 1.13$
MGRO J2031+41	72.1	$4.8 \pm 0.9 \pm 1.4$	$14.1 \pm 3.2 \pm 5.3$	$3.16 \pm 0.33 \pm 0.27$
MGRO J2228+61	114	$2.9 \pm 0.5 \pm 0.5$	$8.5 \pm 2.0 \pm 1.5$	$3.21 \pm 0.43 \pm 0.27$
VER J0006+727	1205.6	$12.4 \pm 1.0 \pm 1.8$	$30.4 \pm 2.7 \pm 5.3$	$3.85 \pm 0.22 \pm 0.24$
VER J2016+372	31.4	$1.8 \pm 0.5 \pm 1.0$	$7.3 \pm 2.8 \pm 5.3$	$2.45 \pm 0.44 \pm 0.21$

Note. — Results of the maximum likelihood spectral fits for LAT-detected TeV sources. The test statistic (TS) for the source significance is provided in column 2. Columns 3 and 4 list the photon flux F(10–316 GeV) and the energy flux G(10–316 GeV). The fits used the best morphology reported in Table 5 and a power-law spectral model (see Equation 2) with photon index Γ given in column 5. The uncertainties on F(10–316 GeV), G(10–316 GeV), and Γ correspond respectively to the statistical and systematics uncertainties (see Section 4.7).

Table 7. Spectral fitting results for LAT-detected TeV sources in three energy bands logarithmically-spaced

TeV source	TS (10–31 GeV)	F(10–31 GeV) (10^{-10} ph cm^{-2} s^{-1})	TS (31–100 GeV)	F(31–100 GeV) (10^{-11} ph cm^{-2} s^{-1})	TS (100–316 GeV)	F(100–316 GeV) (10^{-11} ph cm^{-2} s^{-1})
HESS J1018-589	24.7	1.3 ± 0.5 ± 0.5	0.5	< 5.9	5.7	< 6.2
HESS J1023-575	42.8	3.7 ± 0.8 ± 1.4	1.6	< 9.0	18.3	1.8 ± 0.5 ± 0.9
HESS J1119-614	17.1	1.6 ± 0.5 ± 0.5	1.0	< 7.5	11.0	1.3 ± 0.6 ± 0.6
HESS J1303-631	20.9	3.6 ± 0.9 ± 1.4	26.6	17.1 ± 0.5 ± 0.6	7.8	< 10.7
HESS J1356-645	0.2	< 9.4	14.7	1.4 ± 0.7 ± 0.4	10.7	6.5 ± 1.7 ± 1.7
HESS J1418-609	28.7	3.7 ± 0.9 ± 1.2	1.7	< 10.5	0.2	< 5.4
HESS J1420-607	18.1	2.4 ± 0.7 ± 0.7	12.0	6.8 ± 2.6 ± 3.0	12.0	4.0 ± 1.7 ± 2.1
HESS J1507-622	18.2	1.4 ± 0.4 ± 0.4	2.8	< 7.0	0.5	< 3.9
HESS J1514-591	69.6	3.9 ± 0.7 ± 1.0	65.7	15.8 ± 3.9 ± 4.8	36.8	6.7 ± 2.5 ± 2.7
HESS J1614-518	73.4	7.9 ± 1.2 ± 2.6	52.4	27.6 ± 5.9 ± 11.6	27.1	9.1 ± 3.2 ± 4.6
HESS J1616-508	46.8	6.5 ± 1.2 ± 2.0	28.4	19.9 ± 5.4 ± 9.5	4.0	< 10.1
HESS J1632-478	71.2	10.3 ± 1.5 ± 4.2	38.1	28.2 ± 6.4 ± 11.4	37.6	15.4 ± 4.4 ± 6.3
HESS J1634-472	15.5	3.6 ± 1.0 ± 1.9	11.7	10.8 ± 3.7 ± 5.7	2.1	< 8.3
HESS J1640-465	20.1	3.4 ± 0.9 ± 1.5	32.2	15.1 ± 4.5 ± 6.9	0	< 4.5
HESS J1708-443	1131.3	22.0 ± 1.5 ± 3.2	22.0	5.0 ± 1.3 ± 2.0	0.0	< 6.3
HESS J1804-216	83.7	9.6 ± 1.4 ± 2.5	37.1	24.6 ± 6.1 ± 10.7	20.8	10.4 ± 3.9 ± 5.1
HESS J1825-137	18.2	6.4 ± 1.7 ± 3.4	46.7	50.5 ± 9.4 ± 20.4	19.4	11.9 ± 4.4 ± 5.5
HESS J1834-087	21.9	4.4 ± 1.6 ± 1.9	7.0	< 18.7	2.5	< 9.7
HESS J1837-069	30.6	6.9 ± 1.4 ± 3.1	24.3	25.6 ± 6.7 ± 10.5	28.3	15.2 ± 4.6 ± 5.9
HESS J1841-055	22.8	6.4 ± 1.6 ± 3.0	11.0	19.6 ± 7.1 ± 5.7	22.1	14.5 ± 4.5 ± 7.0
HESS J1848-018	16.0	5.8 ± 1.6 ± 3.1	4.2	< 26.0	0.4	< 10.1
HESS J1857+026	1.9	< 2.5	12.9	13.8 ± 4.5 ± 6.8	39.3	13.0 ± 4.5 ± 4.6
MGRO J0632+17	2144.4	27.6 ± 1.6 ± 9.8	13.0	3.0 ± 1.0 ± 1.7	0	< 3.8
MGRO J1908+06	32.1	2.6 ± 0.5 ± 1.2	0.0	< 5.0	2.8	8.6
MGRO J1958+2848	18.9	1.3 ± 0.5 ± 0.4	0	< 3.3	0	<3.0
MGRO J2019+37	100.1	3.7 ± 0.7 ± 1.5	0	< 3.2	2.4	< 4.9
MGRO J2031+41	66.7	4.6 ± 0.8 ± 1.3	5.2	< 9.4	0	< 3.6
MGRO J2228+61	108.8	2.7 ± 0.5 ± 0.5	8.0	< 7.0	0	<2.3
VER J0006+727	1181.0	12.3 ± 0.9 ± 2.0	38.4	3.9 ± 1.6 ± 1.6	1.5	< 3.2
VER J2016+372	25.9	1.6 ± 0.4 ± 0.5	3.4	< 5.9	3.2	< 5.0

Note. — Results of the maximum likelihood spectral fits for LAT-detected TeV sources in three different energy bands: 10–31 GeV, 31–100 GeV, 100–316 GeV using the same convention as in Table 6. A 99% c.l. upper limit is computed when the TS in the band is lower than 10.

Table 8. Upper limits for non-detected TeV sources above 10 GeV

TeV source	TS	F(10–316 GeV) $(10^{-10}$ ph cm^{-2} s$^{-1})$	G(10–316 GeV) $(10^{-12}$ erg cm^{-2} s$^{-1})$
HESS J1026-582	1.0	< 1.6	< 9.3
HESS J1427-608	4.4	< 2.0	< 11.4
HESS J1458-608	12.6	< 2.5	< 14.5
HESS J1503-582	9.8	< 3.9	< 22.3
HESS J1554-550	0	< 0.5	< 2.8
HESS J1626-490	1.5	< 2.7	< 15.4
HESS J1702-420	8.5	< 6.8	< 38.9
HESS J1718-385	2.9	< 2.5	< 14.6
HESS J1729-345	0	< 1.3	< 7.6
HESS J1809-193	10.4	< 11.0	< 63.4
HESS J1813-178	2.5	< 2.4	< 14.2
HESS J1818-154	0	< 1.4	< 8.1
HESS J1831-098	0	< 1.8	< 10.6
HESS J1833-105	4.1	< 2.1	< 11.7
HESS J1843-033	0	< 1.0	< 5.4
HESS J1846-029	2	< 2.0	< 11.2
HESS J1849-000	0.1	< 1.3	< 7.3
HESS J1858+020	0	< 1.2	< 6.6
HESS J1912+101	9.5	< 4.5	< 25.2
MGRO J0631+105	5.9	< 1.4	< 7.7
MGRO J1844-035	0	< 1.4	< 8.0
MGRO J1900+039	0	< 1.2	< 6.9
MGRO J2031+41	14.7	< 30.0	< 168.9
VER J1930+188	0	< 1.0	< 5.5
VER J1959+208	0	< 0.3	< 1.9
W49 A	3.2	< 2.4	< 37.6

Note. — Results of the maximum likelihood spectral fits for non-detected TeV sources. The test statistic (TS) for the source significance is provided in column 2. Columns 3 and 4 list the 99% c.l. upper limits on the photon flux F(10–316 GeV) and on the energy flux G(10–316 GeV). The fits used the TeV template defined in Table 1 and a power-law spectral model (see Equation 2) with photon index fixed at 2.

– 35 –

Table 9. Upper limits for non-detected TeV sources in three energy bands logarithmically-spaced between 10 and 316 GeV

TeV source	TS (10–31 GeV)	F(10–31 GeV) (10^{-10} ph cm^{-2} s^{-1})	TS (31–100 GeV)	F(31–100 GeV) (10^{-11} ph cm^{-2} s^{-1})	TS (100–316 GeV)	F(100–316 GeV) (10^{-11} ph cm^{-2} s^{-1})
HESS J1026-582	0.5	< 1.6	0.0	< 3.6	0.6	< 7.4
HESS J1427-608	0.3	< 1.3	2.6	< 9.0	3.3	< 6.2
HESS J1458-608	12.3	1.7 ± 0.5 ± 0.7	0.4	< 5.0	0.0	< 3.4
HESS J1503-582	0.9	< 2.2	4.3	< 14.8	5.2	< 9.9
HESS J1554-550	0.0	< 0.6	0.0	< 3.3	0.0	< 2.8
HESS J1626-490	0.7	< 2.2	0.9	< 10.7	0.0	< 7.2
HESS J1702-420	0.3	< 3.3	7.9	< 36.2	1.0	< 10.7
HESS J1718-385	0.2	< 1.7	0.3	< 8.9	3.0	< 10.2
HESS J1729-345	0.0	< 1.4	0.0	< 7.5	0.0	< 4.5
HESS J1809-193	8.4	< 9.3	3.3	< 32.4	0.0	< 11.5
HESS J1813-178	0.0	< 1.4	3.0	< 16.3	0.5	< 7.1
HESS J1818-154	0.0	< 1.5	0.0	< 7.8	0.0	< 4.4
HESS J1831-098	0.0	< 1.5	0.1	< 10.1	0.2	< 6.2
HESS J1833-105	3.1	< 1.9	1.2	< 7.1	0.0	< 6.5
HESS J1843-033	0.0	< 1.0	0.0	< 4.9	0.0	< 5.3
HESS J1846-029	2.1	< 2.3	0.0	< 5.2	0.0	< 4.1
HESS J1849-000	0.2	< 1.4	0.0	< 4.8	0.0	< 4.7
HESS J1858+020	0.0	< 1.2	0.0	< 6.4	0.0	< 4.0
HESS J1912+101	0.9	< 2.4	6.9	< 19.5	3.2	< 10.7
MGRO J0631+105	3.5	< 1.2	3.2	< 6.1	0.0	< 3.6
MGRO J1844-035	0.0	< 1.1	0.4	< 2.5	0.0	< 3.5
MGRO J1900+039	0.0	< 1.4	0.0	< 6.3	0.0	< 4.4
MGRO J2031+41	8.7	< 22.6	6.1	< 83.6	0.9	< 22.8
VER J1930+188	0.7	< 1.1	0.0	< 4.4	0.0	< 3.1
VER J1959+208	0.0	< 0.3	0.0	< 2.9	0.0	< 3.9
W49 A	3.0	< 5.5	0.5	< 16.4	0.0	< 8.0

Note. — Results of the maximum likelihood spectral fits for non-detected TeV sources in three different energy bands: 10–31 GeV, 31–100 GeV, 100–316 GeV using the same convention as in Table 8. A 99% c.l. upper limit is computed when the TS in the band is lower than 10.
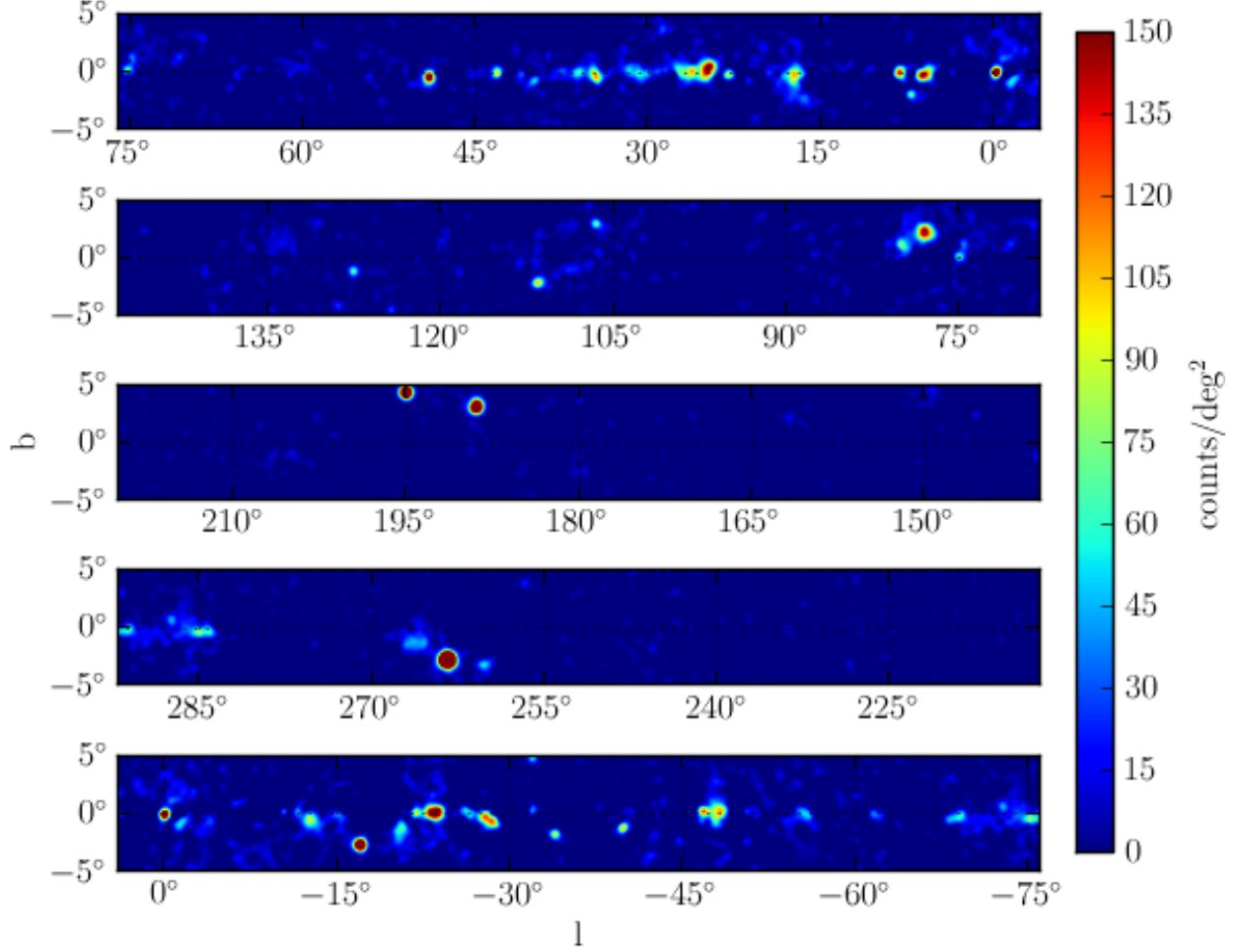
Fig. 1.— Residual counts map of the Galactic Plane above 10 GeV. The galactic and isotropic diffuse emission are subtracted using the files described in section 4.2 with a normalization of 1. All sources associated to Blazars are subtracted using the spectral parameters listed in the hard source list(+ citer Hard source list). Excesses visible in this map are due to Galactic sources emitting above 10 GeV observed by the LAT. The counts map is smoothed with a Gaussian of 0.27°.

Table 10.   Spectral results for sources with a γ-ray detected pulsar within $0.5°$ with the pulsar included in the model

Source name	TS	F(10-316 GeV) $(10^{-10}$ ph cm^{-2} s$^{-1})$	Index	shape
HESS J1018-589	25.0	$1.5 \pm 0.5_{stat}$	$2.31 \pm 0.5_{stat}$	TeV
HESS J1023-577	51.2	$4.5 \pm 0.9_{stat}$	2.04 ± 0.26	TeV
HESS J1119-614	16.0	$1.5 \pm 0.6_{stat}$	$1.80 \pm 0.48_{stat}$	TeV
HESS J1356-645	25.4	$1.2 \pm 0.4_{stat}$	$1.00 \pm 0.38_{stat}$	TeV
HESS J1418-609	12.6	< 4.4	-	TeV
HESS J1420-607	35.8	$3.4 \pm 0.9_{stat}$	$1.80 \pm 0.29_{stat}$	TeV
HESS J1458-608	11.0	$<2.5e-10$	-	TeV
HESS J1708-443	62.7	$8.3 \pm 1.5_{stat}$	$3.16 \pm 0.34_{stat}$	point-like
HESS J1718-385	2.9	< 2.5	-	TeV
HESS J1804-216	121.0	$13.1 \pm 1.6_{stat}$	$2.00 \pm 0.16_{stat}$	TeV
HESS J1833-105	4.1	<2.1	-	TeV
MGRO J0631+105	2.5	< 1.0	-	TeV
MGRO J0632+17	128.4	$12.5 \pm 1.5_{stat}$	$4.09 \pm 0.33_{stat}$	point-like
MGRO J1908+06	9.0	< 5.5	-	TeV
MGRO J1958+2848	18.6	$1.2 \pm 0.4_{stat}$	$3.9 \pm 1.0_{stat}$	point-like
MGRO J2019+37	16.8	$2.1 \pm 0.8_{stat}$	$4.61 \pm 0.76_{stat}$	point-like
MGRO J2228+61	18.4	$1.5 \pm 0.5_{stat}$	$2.58 \pm 0.49_{stat}$	point-like
VER J0006+727	27.9	$3.1 \pm 0.9_{stat}$	2.79 ± 0.36	point-like

Note. — Results of the maximum likelihood spectral fits for sources with a known γ-ray pulsar within $0.5°$. The pulsar is included in the model with the spectral parameters derived in the 2FGL catalog Nolan et al. (2012). A 99% c.l. upper limit is computed when the TS is lower than 16. As PSR J1028-5819 is already included and fitted in our model of the region of HESS J1026-5819 we did not report it in this table. PSR J1513-5908 and PSR J1702-4128 were detected after the 2FGL catalog analysis (Nolan et al. 2012). Thus no spectral parameters were available.
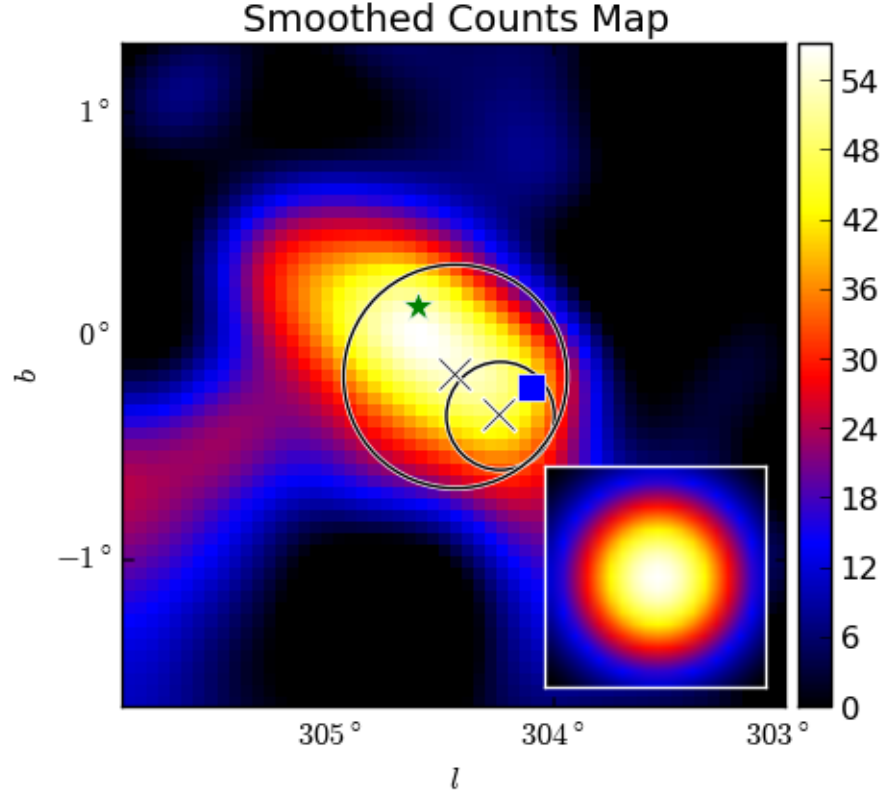
Fig. 2.— Counts map of the region of HESS J1303–631. We subtracted the Galactic and isotropic diffuse emission. The counts map is smoothed by a 0.27° gaussian corresponding to the PSF above 10 GeV. The green star show the position of the SNR Kes 17, the blue square represent the position of PSR J1301–6305. The small and big circles respectively show the extension of TeV gaussian proposed by Aharonian et al. (2005c) and the extension of the disk derived in this work.
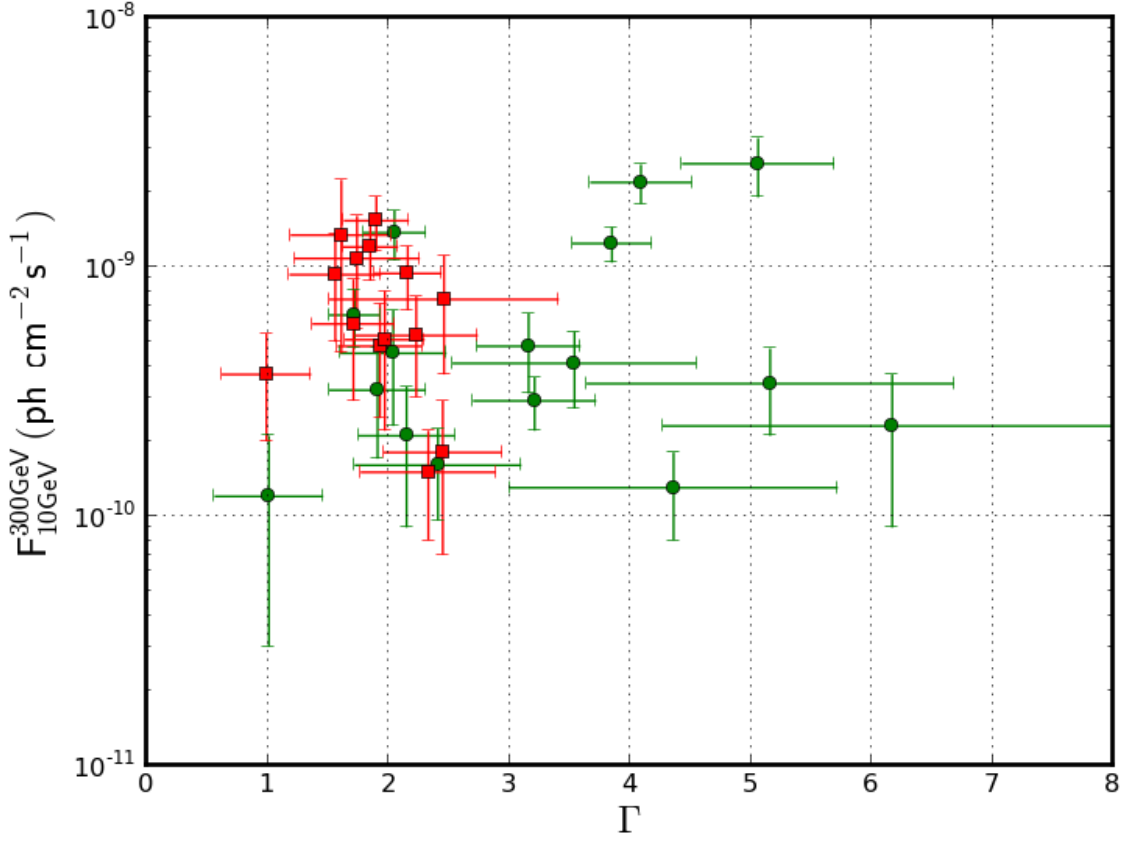
Fig. 3.— Integrated flux of the detected sources as a function of the power-law index between 10 and 316 GeV. The green circles show the sources associated to pulsar detected by the LAT while the red squares represents the sources without pulsar detected in GeV energy ranges. The error bar shows the statistical and systematic uncertainties added in quadrature.
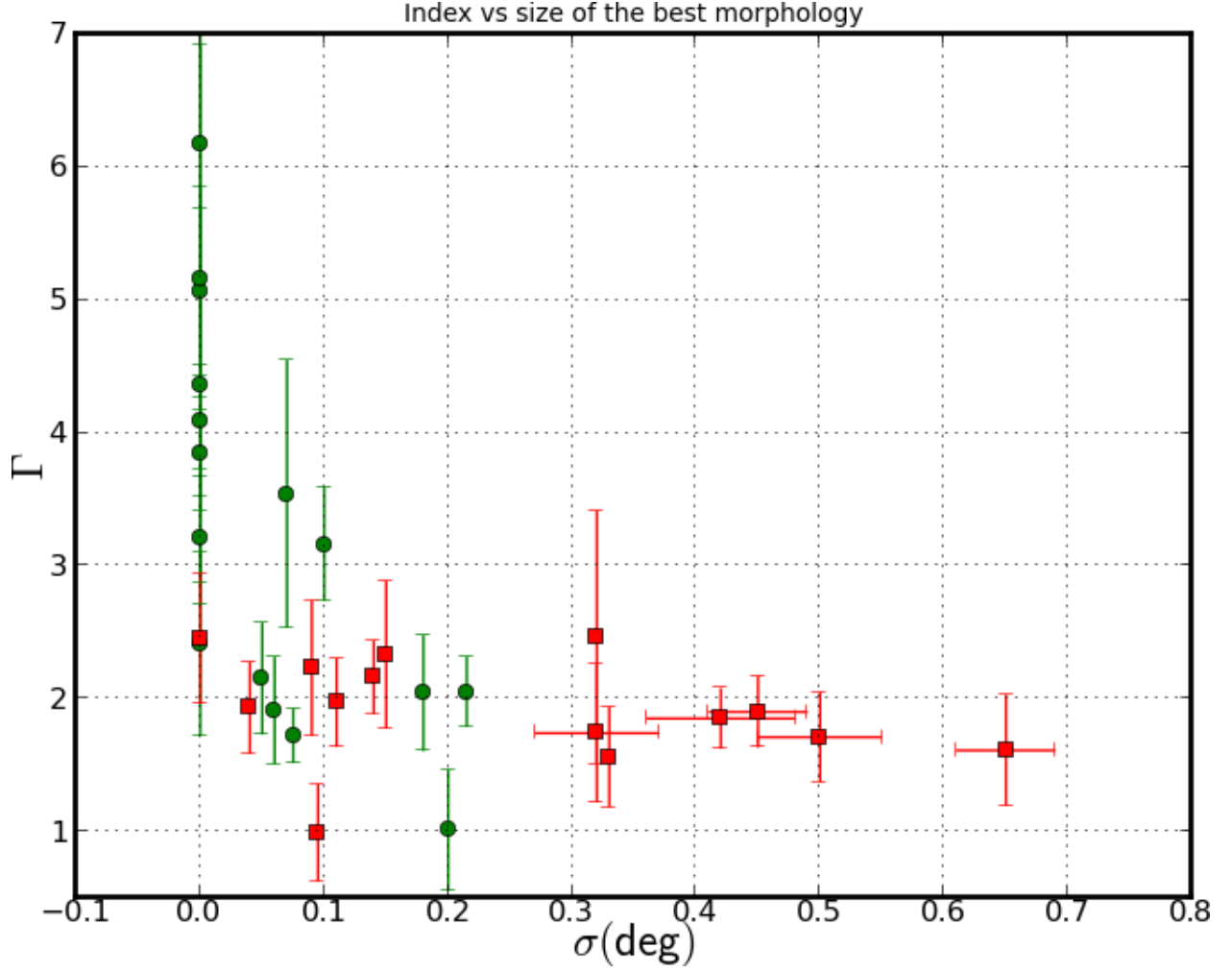
Fig. 4.— Index of the sources as a function of the extension found for each detected source. The green circles show the sources associated to pulsar detected by the LAT while the red squares represents the sources without pulsar detected in GeV energy ranges. The error bar shows the statistical and systematic uncertainties added in quadrature.
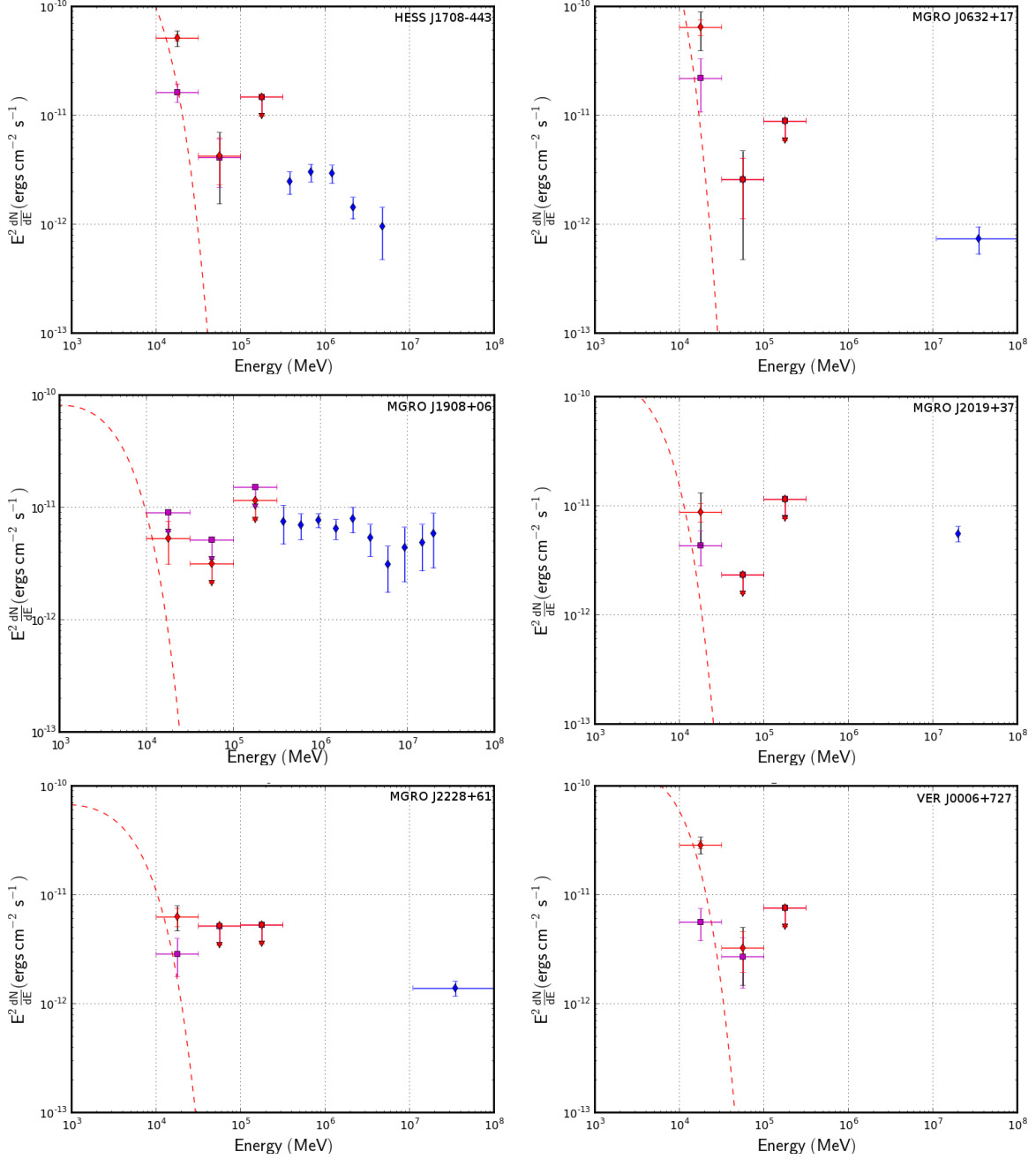
Fig. 5.— SED of the sources better described by a point–like source and with a pulsar within 0.5°. The blue points show the TeV points taken from **Add the papers**. The red circles and the magenta squares show respectively the SED without the pulsar included in the model and with the pulsar included in the model. The black error bars show the statistical and systematic uncertainties added in quadrature. The dashed line correspond to the model of the associated pulsars sumarized in 10 taken from Nolan et al. (2012). In the case of MGRO J1908+06, the red SED was derived assuming a point-like source as determined in tab. 5 while the magenta SED was derived assuming the TeV shape.
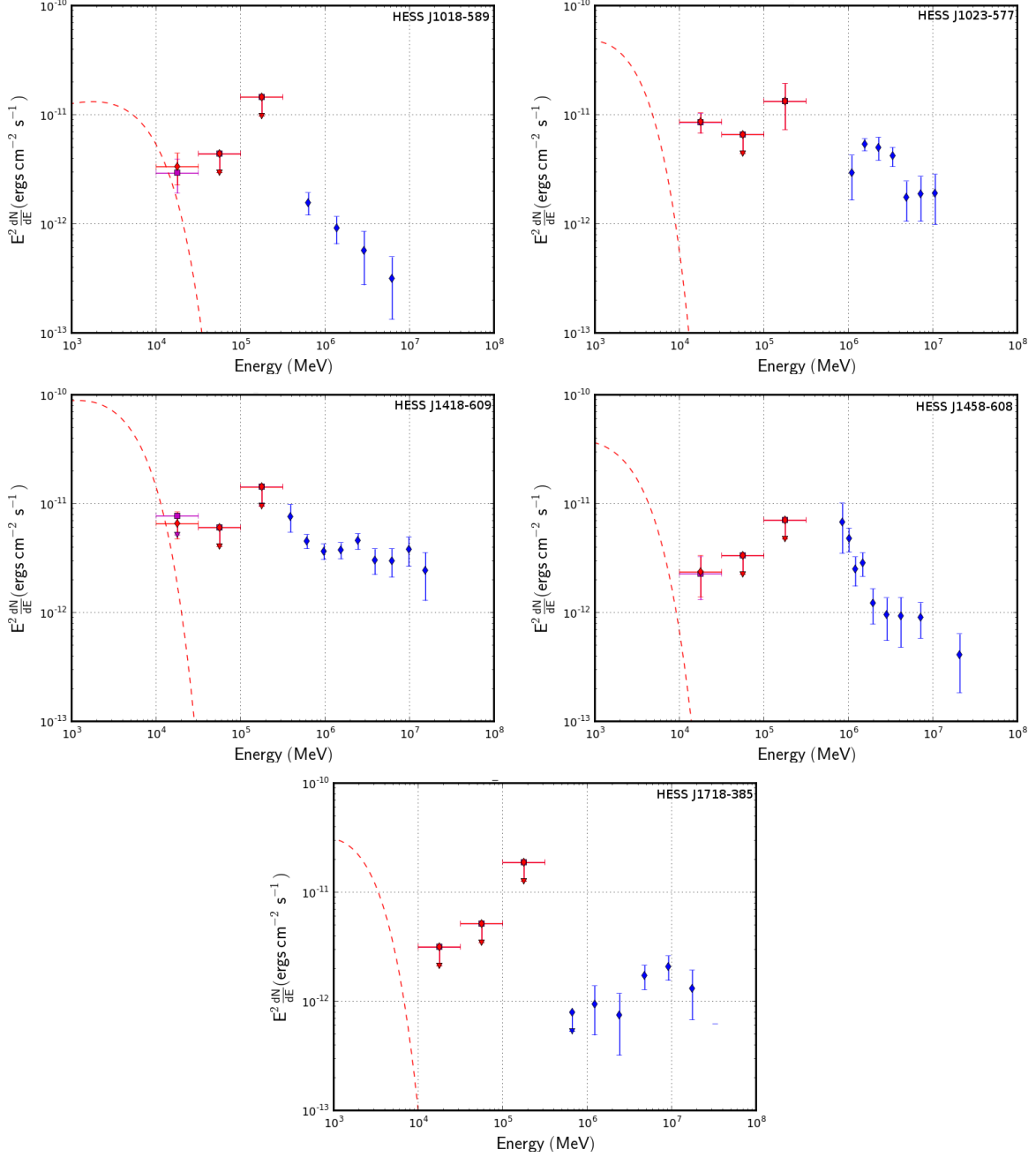
Fig. 6.— SED of the sources better described by the TeV shape and with a pulsar within 0.5°. The blue points show the TeV points taken from **rajouter tous les papiers**. The red circles and the magenta squares show respectively the SED without the pulsar included in the model and with the pulsar included in the model. The black error bars show the statistical and systematic uncertainties added in quadrature. The dashed line correspond to the model of the associated pulsars sumarized in 10 taken from Nolan et al. (2012).
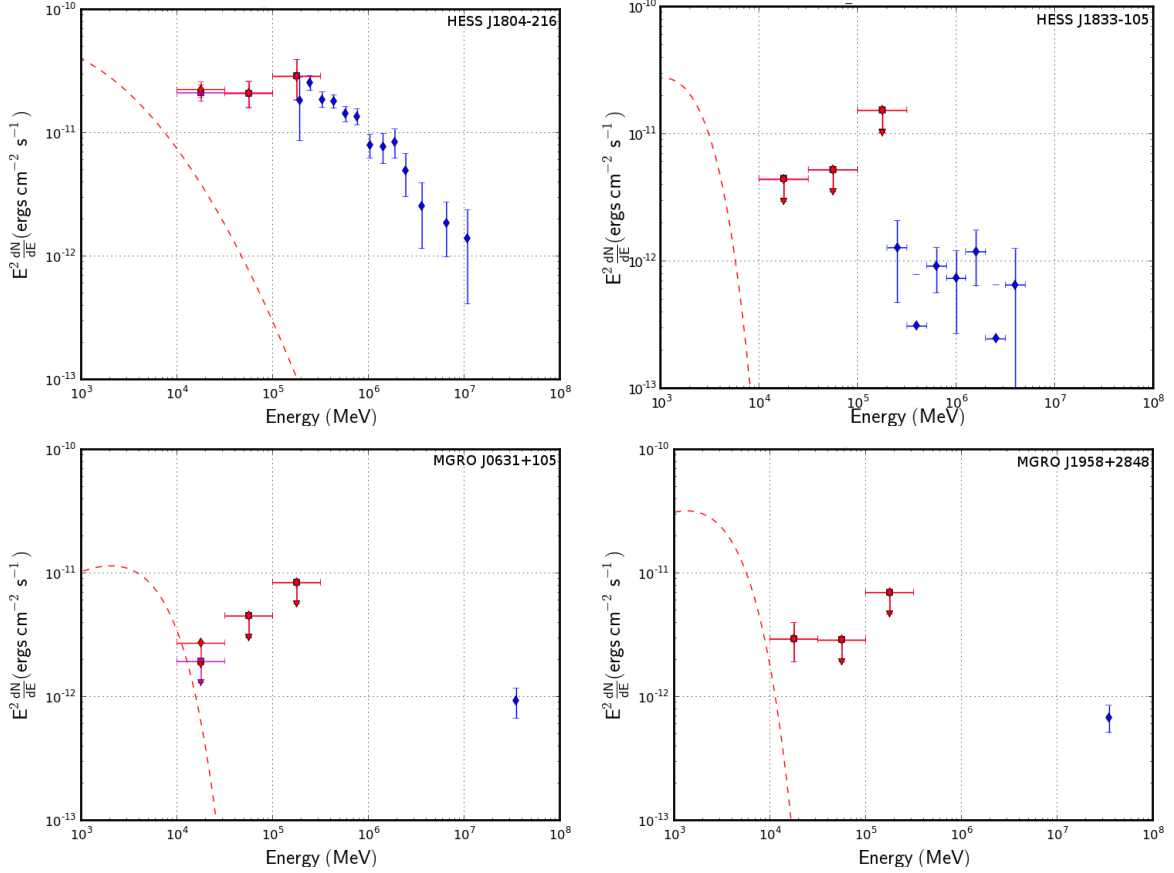
Fig. 7.— SED of the sources better described by the TeV shape and with a pulsar within 0.5°. The blue points show the TeV points taken from **rajouter tous les papiers**. The red circles and the magenta squares show respectively the SED without the pulsar included in the model and with the pulsar included in the model. The black error bars show the statistical and systematic uncertainties added in quadrature. The dashed line correspond to the model of the associated pulsars sumarized in 10 taken from Nolan et al. (2012).
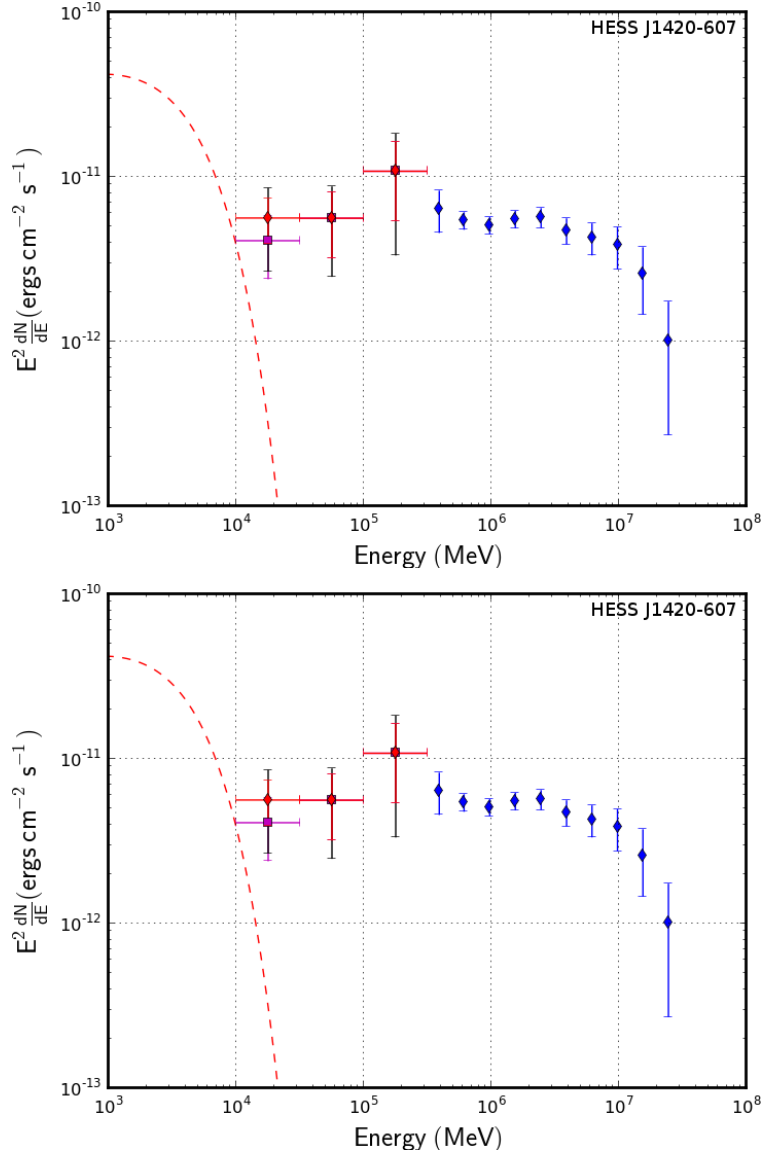
Fig. 8.— SED of . Top : Leptonic scenario. Bottom : Hadronic scenario.
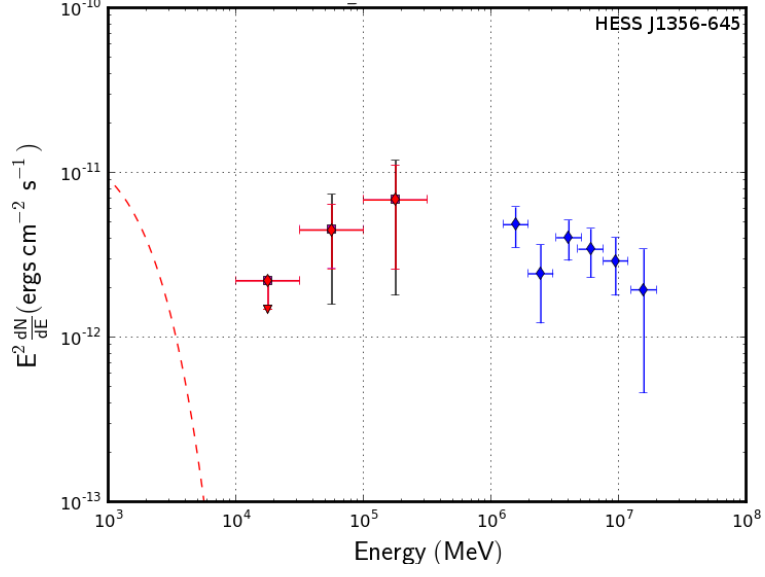
Fig. 9.— SED of
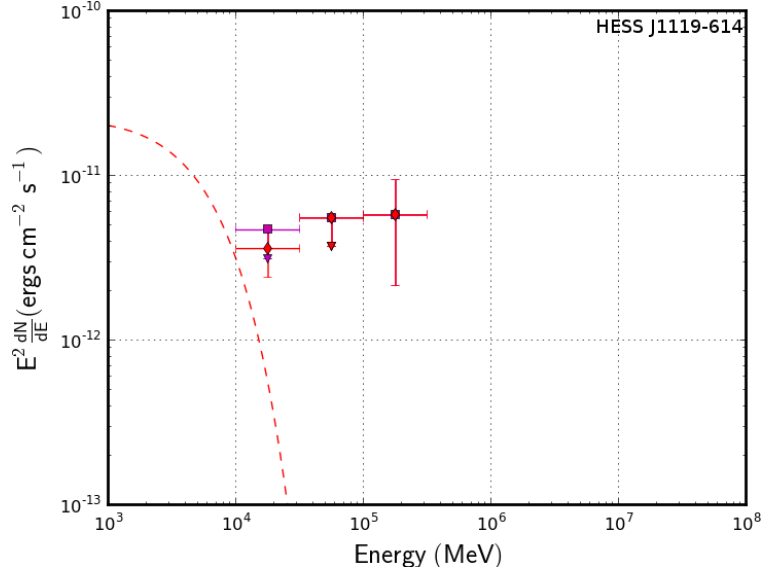
Fig. 10.— SED of
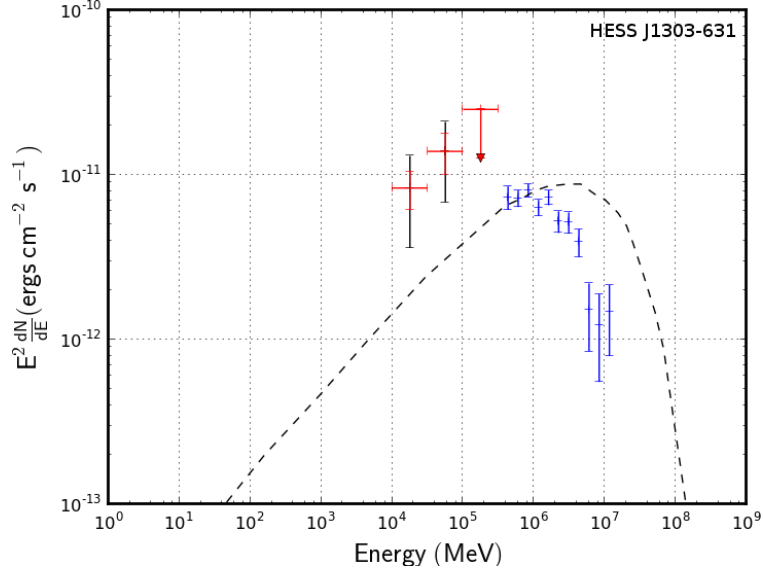
Fig. 11.— SED of
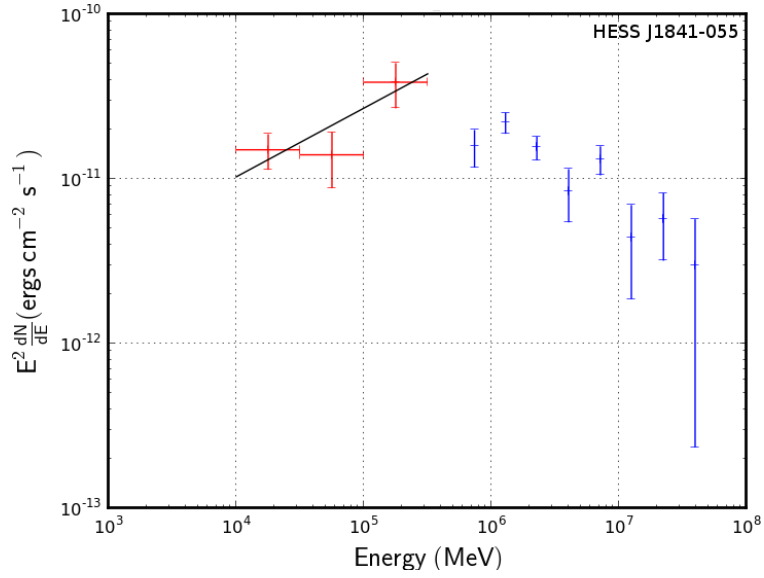
Fig. 12.— SED of HESS J1841-055
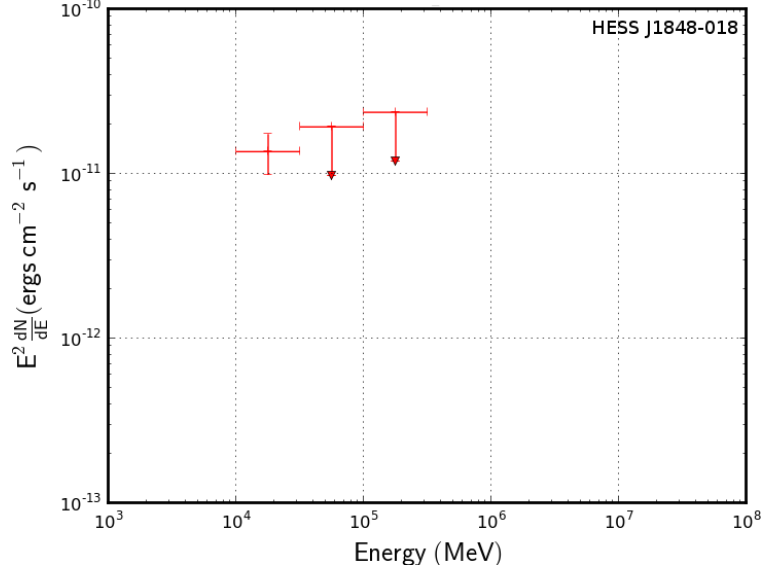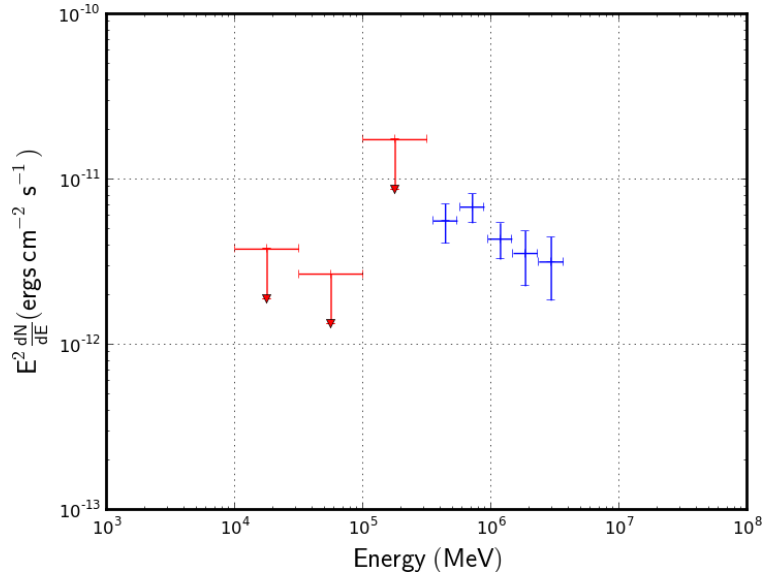
Fig. 13.— SED of HESS J1848
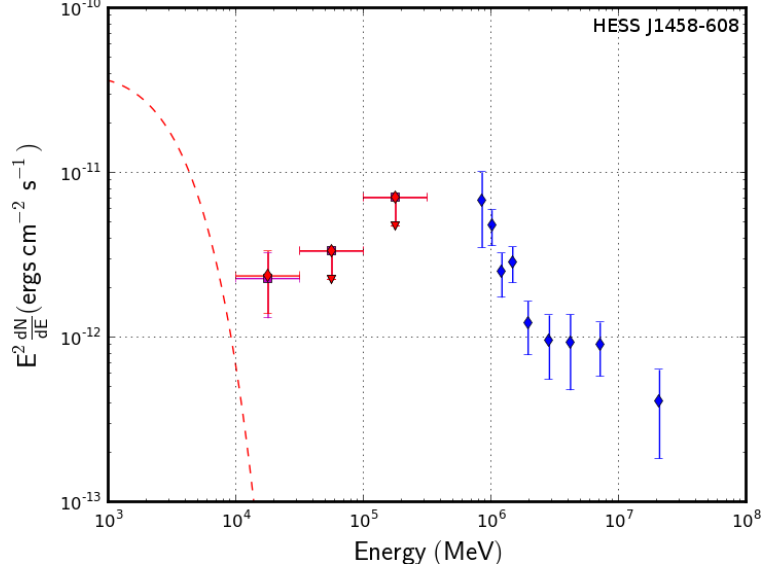

Fig. 14.— SED of HESS J1026 With SED model

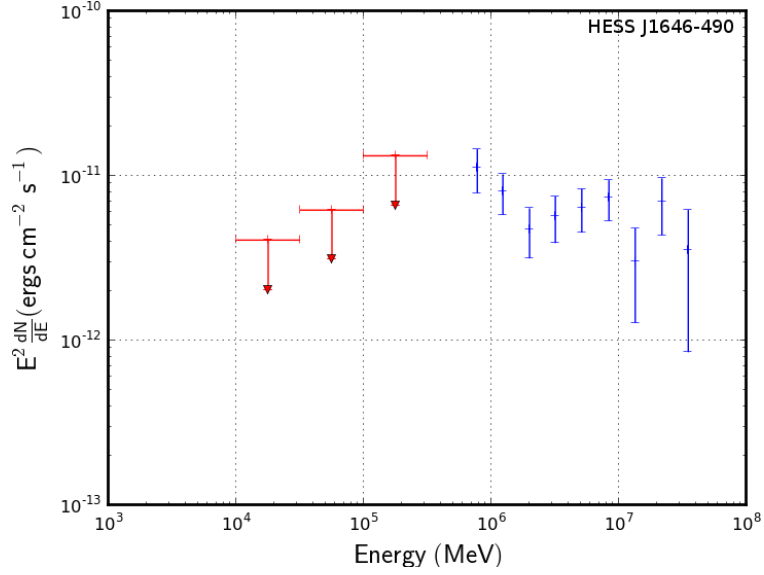Fig. 15.— SED of HESS J1458 With SED model
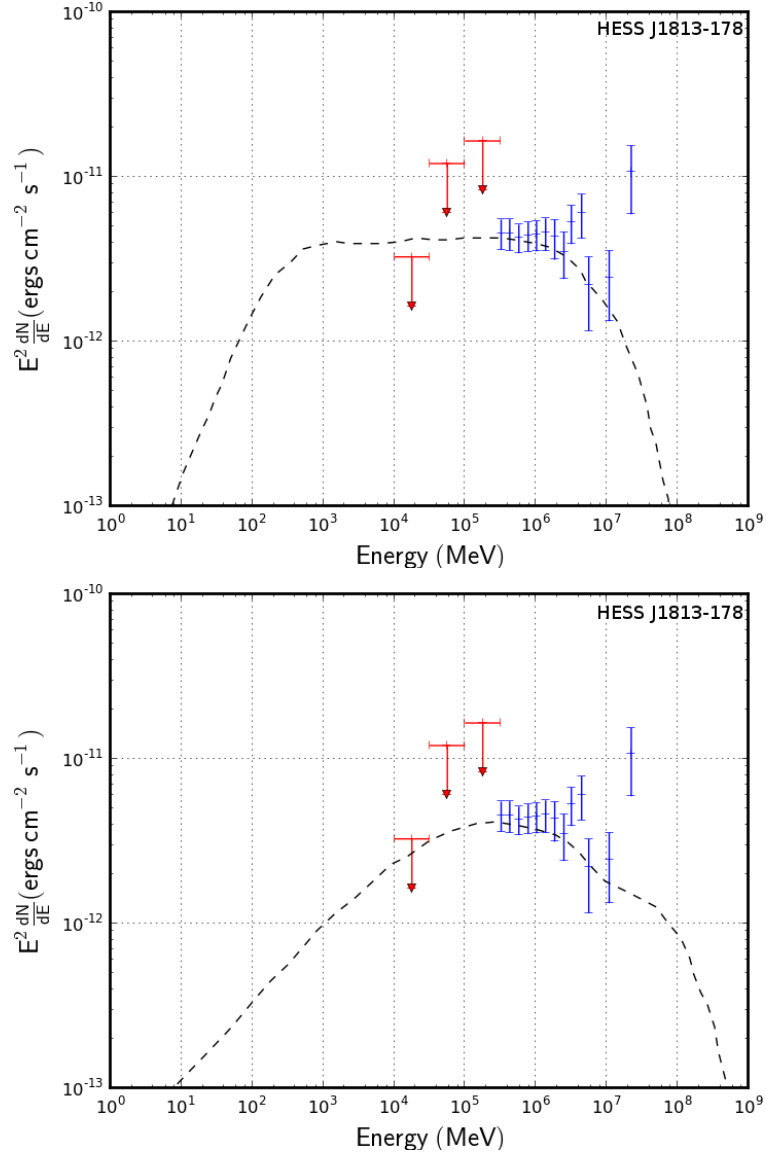

Fig. 16.— SED of HESS J1626 With SED model

Fig. 17.— SED of . Top : Leptonic scenario. Bottom : Hadronic scenario.